minerals

Article

Formation and Tectonic Evolution of Ophiolites in the Sabah Area (Borneo, SE Asia)

Zhiwen Tian, Youfeng Gao, Pujun Wang and Huafeng Tang *

College of Earth Sciences, Jilin University, Changchun 130061, China; tianzw21@mails.jlu.edu.cn (Z.T.); gaoyoufeng@jlu.edu.cn (Y.G.); wangpj@jlu.edu.cn (P.W.)
* Correspondence: tanghfhc@jlu.edu.cn; Tel.: +86-13086803020

Abstract: Zircon U-Pb dating, rock geochemistry, Sr-Nd-Pb, and zircon Hf isotope analyses were conducted on the ultrabasic and basic rocks of ophiolites in the Sabah area (Borneo, SE Asia). The zircon U-Pb ages of ultrabasic and basic rocks range from 248 to 244 Ma, indicating that the ophiolites already existed in the early Triassic. The rare earth elements of basic rocks in Central Sabah show N-MORB-type characteristics and E-MORB-type characteristics in the northwest and southeast. The $\varepsilon_{\mathrm{Nd}}(t)$ values of basic rocks range from 3.66 to 8.73, and the $\varepsilon_{\mathrm{Hf}}(t)$ values of zircon in ultrabasic rocks are between −10.2 and −6.1. Trace element analysis shows that the magmatic source was influenced by melts and fluids from the subducting plate of the Paleo-Tethys Ocean. The tectonic evolution of the Sabah area can be traced back to the Early Triassic. At that time, the fast subduction of the Paleo-Tethys Ocean plate and the retreating of the Paleo-Pacific plate resulted in the upwelling of mantle material in relatively small extensional settings, leading to the formation of the ophiolites. From the Jurassic to the Early Cretaceous, the Paleo-Pacific plate was intensely subducted, and the ophiolite intrusion in the Sabah area moved to the continental crust of South China or the Sundaland margin as fore-arc ophiolites. From the Late Cretaceous to the Miocene, with the expansion of the Proto-South China Sea and South China Sea oceanic crust, the ophiolites in the Sabah area drifted southward with microplate fragments and sutured with East Borneo.

Keywords: Borneo; Sabah; Early Triassic ophiolites; tectonics; Paleo-Tethys Ocean

check for updates

Citation: Tian, Z.; Gao, Y.; Wang, P.; Tang, H. Formation and Tectonic Evolution of Ophiolites in the Sabah Area (Borneo, SE Asia). *Minerals* **2024**, *14*, 1078. https://doi.org/10.3390/min14111078

Academic Editors: Basilios Tsikouras, Paola Tartarotti and Ruibao Li

Received: 31 August 2024
Revised: 18 October 2024
Accepted: 23 October 2024
Published: 25 October 2024

1. Introduction

Ophiolites are fragments of non-in situ upper mantle and pristine oceanic crust that exhibit diversity in rock assemblages, magma evolution, source composition, formation environments, emplacement mechanisms, and the degree of late tectonic reworking [1–3]. Ophiolites are of great interest in restoring plate movements and tectonic evolution processes [4–7]. The Southeast Asian region underwent multiple plate collisions and stacking during the Mesozoic and Cenozoic and the influence of the Tethys and Pacific tectonic domains [8–12]. Consequently, many ophiolites were distributed along the suture zone in the Indo-China Peninsula, Philippines, Borneo, Sulawesi, and Sumatra–Java regions (Figure 1) [13,14]. Borneo was also formed by the collision and stacking of multiple small plates, distributed with a large amount of ophiolites, including the Boyan, Lubok Antu, and Kapuas mélanges along the Lupar Line to the west [8,15], Meratus suture melanges to the southeast [16], and in the Sabah area [14,17–19]. The ophiolites distributed along the Lupar Line are believed to have been formed by subduction of the Proto-South China Sea in the Early Cretaceous, while the mélanges distributed along the Meratus suture are thought to be formed by subduction of the Meratus Ocean in the Early Cretaceous [16]. However, little is known about the formation time, emplacement pattern, and tectonic evolution of ophiolites in the Sabah area [14,18,20–26]. Regarding the formation time, it is unknown whether the ophiolites were formed during the Triassic or Cretaceous [14–19,25–27], and whether the formation was earlier than the age of the crystalline basement. Regarding tectonic evolution, it is unknown whether the ophiolites were formed in mid-ocean ridges [18,28,29], with the expansion and emplacement of supra-subduction zones [25,30], and whether the formation was related to the subduction of the Proto-South China Sea [31]. Regarding the emplacement pattern, it is unknown whether any correlation between ophiolites in the Sabah area and the Palawan ophiolites exist and whether the ophiolites in the Sabah area are relics of the oceanic crust of the Paleo-Tethys Ocean or the Paleo-Pacific [32,33]. Based on field geological fieldwork, the formation and tectonic evolution of ophiolites in the Sabah area are discussed in this work through integrated zircon U-Pb and Lu-Hf isotope and bulk-rock geochemical data.

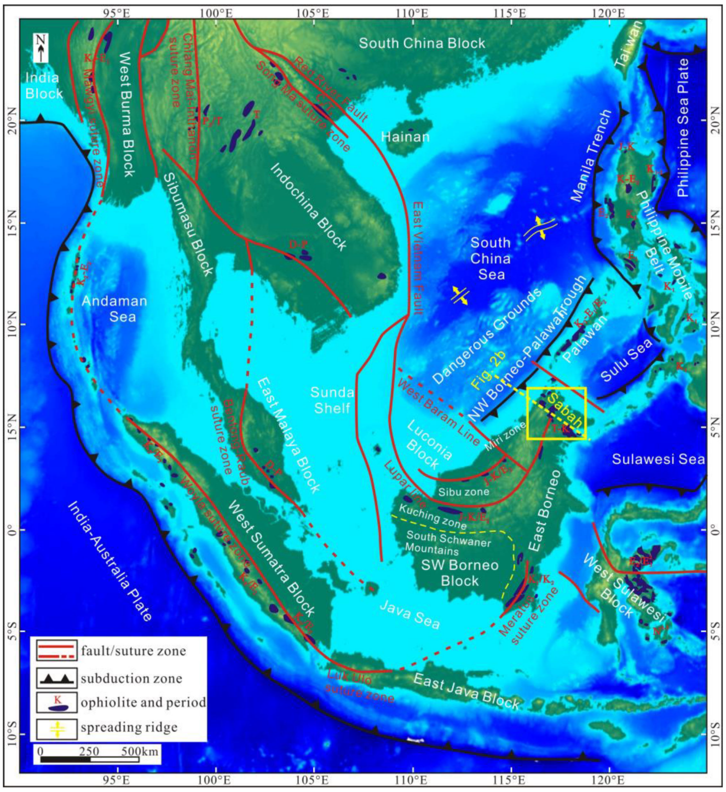

Figure 1. Tectonic sketch map of Southeast Asia [8,13,32]. Yellow square is represented Figure 2a. D, Devonian; P, Permian; P_2, Late Permian; T, Triassic; J, Jurassic; K, Cretaceous; K_1, Early Cretaceous; K_2, Late Cretaceous; E, Paleogene; E_1, Paleocene; E_2, Eocene; E_3, Oligocene; N, Neogene.

2. Geological Setting

2.1. Regional Geological History

The current pattern in Southeast Asia was formed by the suturing of multiple plates during the Mesozoic and Cenozoic. Previous studies have constructed relevant evolution models for the tectonic evolution of multiple plates in Southeast Asia during the Mesozoic and Cenozoic [11,12,32–35]. In the Early to Middle Triassic, the Indochina, East Malaysia, Southern Qiangtang, Northern Qiangtang, Sibumasu, and West Sumatra blocks fractured and drifted northward from the Gondwana continent [9,10]. In the Late Triassic, the Paleo-Tethys Ocean subducted and closed, and these blocks amalgamated with the Jinsha River–Ailaoshan, Song Ma, Longmuco–Shuanghu, Lancang River, Changning–Menglian, and Wendong suture zones [35–38]. In the Late Jurassic, the Southwest Borneo, East Java–West Sulawesi, and Northwest Sulawesi plates split from the Australian plate and drifted northward, while the Meso-Tethys Ocean gradually disappeared [39]. In the Late Cretaceous, Southwest Borneo had already sutured with the edge of Sundaland and amalgamated with West Borneo. Later, the Woyla Arc collided with the West Sumatra plate, while East Java–West Sulawesi sutured with Southwest Borneo. In the Cenozoic era, many tectonic events occurred in Southeast Asia, such as the subduction and the disappearing of the Proto-South China Sea [33], the extension of the South China Sea basin and the Sulu Sea [40], and the counterclockwise rotation of Borneo [41,42].

Borneo was formed by the collision and amalgamation of multiple blocks during the Mesozoic and Cenozoic, and can be divided into Southwest Borneo, East Borneo, the Kuching Belt, the Sibu Belt, the Miri Belt, and Sabah (Figure 1). Southwest Borneo is believed to be a block that separated from the Australian plate during the Mesozoic era, mainly composed of Mesozoic metamorphic basements and magmatic rocks [43]. Eastern Borneo comprises the Mangkalihat and Paternoster microcontinental fragments [8]. The southern parts of East Borneo and Southwest Borneo are bounded by the Meratus suture, while the northern part and the Kuching Belt are bounded by the Mangkalihat melanges. The Kuching Belt is composed of schist basement and river or marginal marine sediments from the Upper Cretaceous to the Cenozoic, while the Sibu Belt is composed of deep-sea sediments and is bordered by the Lupar Line with the Kuching Belt [44]. The basement of the Miri Belt is a paleo continental crust, overlaid with Cenozoic sediments. The Sibu Belt and Miri Belt are recognized as accretionary wedges of subduction in the Proto-South China Sea [31]. Many ophiolitic melanges are distributed along the suture in Borneo and its neighboring areas (Table 1).

Table 1. Summary of geochemical characteristics of mafic rocks from ophiolites in the Palawan and Borneo area.

Locality	Ophiolitic Complex	Age (Ma)	Method	Geochemical Signature	Tectonic Setting	Reference
Palawan	Central Palawan	40.5–34	K-Ar (Am, Mc); Ar-Ar (Am, Mc); U-Pb (Zr)	MORB to MORB-IAT	Forearc or back-arc basin	[45–47]
	Southern Palawan	103–100	U-Pb (Zr)	MORB-like, IAT, OIB	Forearc or main arc	[46–48]
North Borneo	Northern Sabah, Kudat, Baliojong	136–112	Ar-Ar (Wr); U-Pb (Zr); Radiolarian	MORB-like	Mid-oceanic ridge	[14,27]
	Central Sabah, Telupid	163–42.5	K-Ar; Ar-Ar (Wr); U-Pb (Zr)	MORB-like	Mid-oceanic ridge	[14,49]
	Eastern Sabah, Darvel Bay	231–33.41	K-Ar (Hb, Pl); Ar-Ar (Wr); U-Pb (Zr)	N-MORB, OIB, IAT	Mid-oceanic ridge or forearc	[14,17,18,22,26,30,46,49,50]
West Borneo	Lupar line Complex (Boyan, Lubok Antu, Bunguran, Serabang, Sejingkat)	115–105; 98–77	Ar-Ar (Wr); U-Pb (Zr); Radiolarian	MORB-like	Mid-oceanic ridge	[8,15,16,43,46,51,52]
Southeast Borneo	Meratus Complex	150–115	U-Pb (Zr)	Arc volcanics	Forearc	[16]

Note: Am, Amphibole; Hb, Hornblende; Mc, Mica; Pl, Plagioclase; Wr, whole-rock; Zr, zircon.

2.2. Ophiolites and Crystalline Basement in the Sabah Area

The Sabah area is located in the northwestern part of Borneo and is surrounded by the South China, Sulawesi, and the Sulu Seas (Figure 2a). The Sabah area is mainly composed of crystalline basement, Mesozoic ophiolite, and overlying Cenozoic sedimentary rocks [39,53]. The ophiolitic rocks are mainly distributed in Darvel Bay, Segama Highlands, Telupid, Kinabalu, and Banggi areas. The ophiolite is composed of peridotite, gabbro, basaltic dykes, plagiogranites, and radiolarian chert [22,43–55]. The lithological combination of Cretaceous–Early Tertiary igneous rocks (KET), the Chert–Spilite Formation (Cs), and the Sapulut Formation (Sp) in the western section of Sabah display the characteristics of oceanic crust.

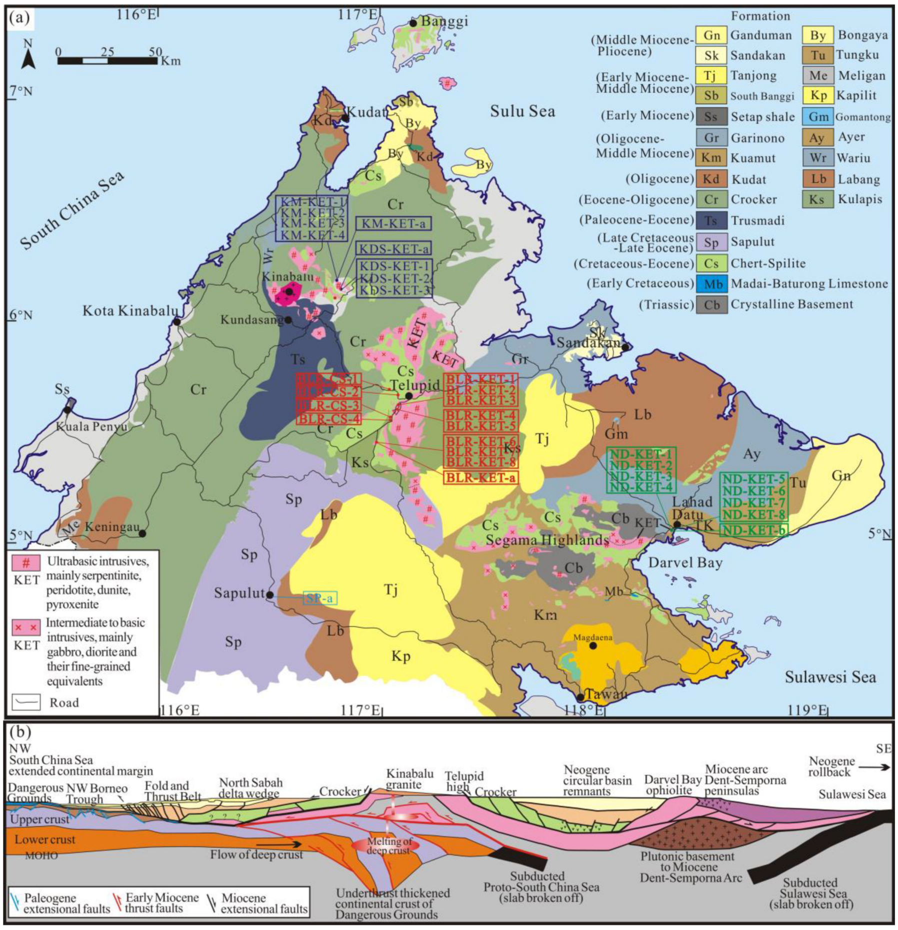

Figure 2. Geological map of the Sabah area and the sample locations ((**a**), location shown in Figure 1), and related cross section (**b**), location shown in Figure 1, reference from Hall (2013) [56].

The lithology of Sp is characterized by deep-sea turbidities (Figure 3a). At the mesoscale, this formation consists of mudstone and siltstone, showing complete Bouma sequences (Figure 3b). Section A consists of a variety of sandstones with graded bedding, with groove casts and scour marks along the bottom surface. Section B is sandstone with parallel bedding. Section C is siltstone with ripple marks and cross-bedding. Section D is horizontally bedded siltstone and silty mudstone. Section E is the overlying massive mudstone. The ratio of sandstone to mudstone is about 0.6 overall, and the stratigraphy was overturned according to the Bouma sequence. In summary, the lithological assemblage represents the deep-sea sediments that cover the oceanic crust.

Cs consist of basic volcanic rocks and deep-sea sedimentary rocks. The sedimentary rocks include chert (Figure 3c,d), mudstones, and a small amount of siltstone. The basic volcanic rocks include gray-black massive basalt, pillow basalt (Figure 3e,f), olivine basalt, and volcanic breccia/tuff. The massive basalt has a porphyritic texture. The phenocrysts include pyroxene and olivine, and the matrix is mostly vitreous–cryptic. The pillow basalt has the characteristic of radial jointing. However, the chilled border of the pillow basalt that would have been caused by alteration and/or weathering is not apparent. The diameters of the pillows are up to 30 cm. The particle size of breccia is 3–6 cm, and the particles are angular in shape, poorly sorted, and non-oriented. The age of the Cs radiolarites of the Telupid ophiolite suite Cs is Early Cretaceous [57]. Under further investigation, the radiolarian chert from other exposed formations yielded age ranges that spanned from the Valanginian to the Turonian [58]. In summary, the lithological combination of this formation represents the basalt layer and deep-sea sedimentary layer of the upper part of the oceanic crust.

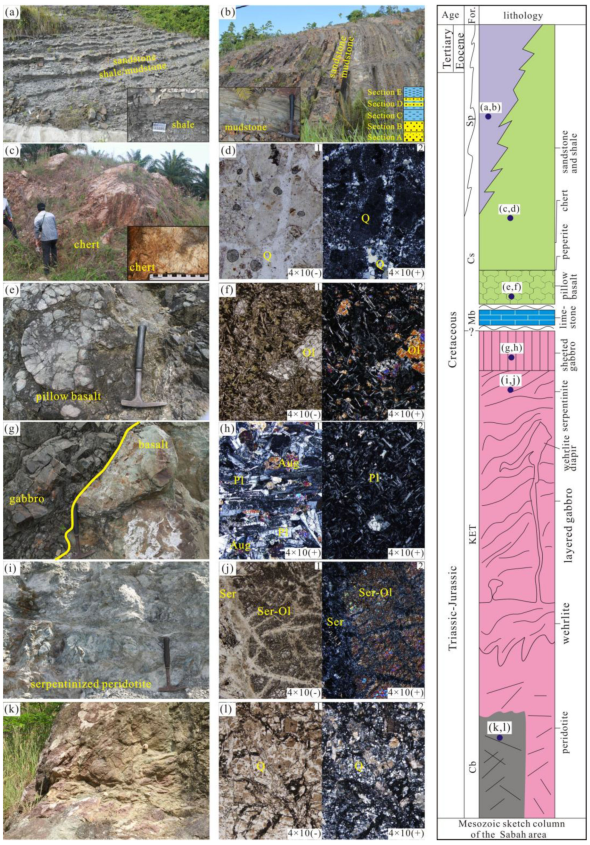

Figure 3. Meso- and microphotographs of the Sabah area. (**a**,**b**) Sp, Bouma sequence, sandstones, shale, and mudstones; (**c**,**d**) radiolarites of Cs; (**e**,**f**) pillow lava and basalts of Cs; (**g**,**h**) KET, gabbro, and basalt; (**i**,**j**) KET, serpentine peridotite; and (**k**,**l**) Cb, cataclastic granite. Aug, Augite; Ol, olivine; Pl, Plagioclase; Q, Quartz; Ser, serpentine.

The KET is dominated by basic and ultrabasic igneous rocks. The basic rocks include gray-black diabase and gabbro (Figure 3g,h), and the ultrabasic rocks include peridotite, and serpentinized peridotite (Figure 3i,j). These rocks registered a strong serpentinization and strong deformation. Tectonic lenses and joints are abundant in the outcrops. The joints are widely filled by calcite veins. In summary, this lithological combination is inferred to represent the characteristics of the middle and lower parts of the oceanic crust.

The crystalline basement is exposed in the Segama Highlands and Darvel Bay in southeastern Sabah. The crystalline basement rocks include gneiss, schist, amphibolite, associated granite (Figure 3k,l), granodiorite, and tonalite. K-Ar and U-Pb zircon age data indicate that the crystalline basement was formed in the Triassic [14,17,22,25,30,50].

The rocks of the Sabah area were deformed during the southward subduction and extinction of the Proto-South China Sea (Figure 2b). The intermediate–mafic igneous rocks are strongly serpentinized. The Cs strata underwent deformation, such as tilting and folding. The entire area was involved in the collisional processes. Their sampling information is summarized and presented in Figure 2a and Table 2.

Table 2. Sampling locations and related information of the Sabah ophiolite.

	Sample	Location	Rock type	Methods
Western Sabah	KM-KET-a	Kimundu (N 6°5′55.5″, E 116°47′56.7″)	Basalt	U-Pb (Zr), Lu-Hf (Zr)
	KM-KET-1–4		Basalt	MT, Sr-Nd-Pb
	KDS-KET-a	Kundasang (N 5°58′22.1″, E 116°44′8.6″)	Serpentinized peridotite (Figure 3i,j)	U-Pb (Zr)
	KDS-KET-1–3		Serpentinized peridotite	MT
Central Sabah	BLR-CS-1–4	Telupid (N 5°39′39″, E 117°2′31.5″)	Basalt (Figure 3e,f)	MT
	BLR-KET-1–3	Telupid (N 5°36′17.5″, E 117°5′50.8″)	Serpentinized peridotite	MT
	BLR-KET-4–5	Telupid (N 5°36′17.0″, E 117°5′49.5″)	Gabbro (Figure 3g,h)	MT
	BLR-KET-a	Tongod (N 5°25′17.0″, E 117°01′23″)	Gabbro	U-Pb (Zr)
	BLR-KET-6–8		Gabbro	MT, Sr-Nd-Pb
Eastern Sabah	ND-KET-b	Lahad Datu (N 5°2′15.9″, E 118°16′7.7″)	Gabbro	U-Pb (Zr)
	ND-KET-1–4		Serpentinized peridotite	MT
	ND-KET-5–8		Basalt	MT
	SP-a	Sapulut (N 4°42′23.4″, E 116°29′24.9″)	Siltstone (Figure 3a,b)	U-Pb (Zr)

Note: Lu-Hf (Zr), zircon Lu-Hf isotopic data; MT, whole-rock major and trace elements; Sr-Nd-Pb, Sr-Nd-Pb isotopic; U-Pb (Zr), zircon U–Pb dating.

3. Analytical Methods

For zircon U-Pb dating analysis, zircon targets, transmitted light images, reflected light images, and cathodoluminescence (CL) images were collected at the College of Earth Sciences, Jilin University, China. Fissureless and inclusion-free areas were delineated on the zircon CL images to ensure the reliability of the data. LA-ICP-MS zircon U-Pb dating was completed at the Key Laboratory of Mineral Resources Evaluation in Northeast Asia, Jilin University. The standard procedure for testing and analysis was conducted on an Agilent7500a ICP-MS instrument (Agilent Technologies, Inc., Santa Clara, CA, USA). During laser denudation, helium gas and argon gas were used as the carrier gas and compensation gas, respectively. The specific experimental steps and instrument parameters were described by [59]. The laser spot size was set to 32 μm, and the zircon standard 91500 was used as the external calibration standard. Data processing was completed using ICPMSDataCal software. The Andersen (2002) method was used to correct for common lead [60]. The age harmonic graph and weighted average age were determined using ISOPLOT 4.15 tools (Ludwig, 2003). In total, five samples (four igneous rock samples and one sandstone sample) were tested.

For zircon Lu-Hf isotope analysis, Lu-Hf isotope analysis was determined with CL images of zircon based on the U-Pb zircon ages obtained in this work. A laser ablation multi-receiver inductively coupled plasma mass spectrometer ((COMPEx GeoLas Pro 193 nm ArF excimer laser (Coherent Corp, Saxonburg, PA, USA) and Neptune Plus (Thermo Fisher Scientific, Waltham, MA, USA)) was used as the testing instrument, with a laser beam of 44 μm, 8 Hz, and ablation time of 26 s, with He gas as the carrier gas. The ^{176}Lu decay constant used in the calculation of $\varepsilon_{Hf}(t)$ was 1.867×10^{-11} yr^{-1}, and the current relevant values of chondrites were ^{176}Hf/^{177}Hf = 0.282785 and ^{176}Lu/^{177}Hf = 0.0336 [61]. The calculation of the Hf depleted mantle model age (TDM1) was conducted based on the current depleted mantle values of ^{176}Hf/^{177}Hf = 0.28325 and ^{176}Lu/^{177}Hf = 0.0384 [62]. Finally, the two-stage Hf model age (TDMC) was calculated using the average continental crust value of ^{176}Lu/^{177}Hf = 0.015 [63].

The major and trace element content of igneous/meta-igneous rock samples was analyzed at the Key Laboratory of Mineral Resources Evaluation in Northeast Asia, Jilin University. The samples were then roughly crushed, and the freshest were selected for cleaning, drying, and grinding to 200 mesh size. The most commonly used analytical method, the X-ray fluorescence (XRF) fused glass method (instrument model: ZSX Primus II) (Rigaku, Tokyo, Japan), was employed to determine the major element contents. For specific experimental techniques, analytical procedures, and testing conditions, we referred to Liu et al. (2002) [64]. Inductively coupled plasma mass spectrometry (ICP-MS) was used to determine the trace element contents. The detailed experimental techniques, experimental parameters, and sample processing steps were described by Liu et al. (2002) [64]. The analytical results for the international standard samples BHVO-1 (basalt) and BCR-2 (basalt) show that the accuracy of the analysis of major elements was better than 5%, whereas the accuracy of the analysis of trace elements was generally better than 10%.

For Sr-Nd-Pb isotope analysis, the samples were treated with acid, washed, dried, and ground to <200 mesh. The analysis was completed at the Key Laboratory of Mineral Resources Evaluation in Northeast Asia, Ministry of Natural Resources. The accurate content of Sr-Nd was determined on Agilent 7700× quadrupole ICP-MS (Agilent Technologies, Inc., Santa Clara, CA, USA). The isotope ratios were measured on Nu PlasmaII MC-ICP-MS (Nu Instruments Ltd., Wrexham, UK). The Pb isotope ratio was measured using a Triton-type thermoelectric ionization mass spectrometer (TIMS) (Thermo Electron, Thermo Fisher Scientific, Waltham, MA, USA). For the isotope ratio determination, NIST SRM 987, JNdi-1, and NBS 981 were selected as Sr, Nd, and Pb standards, respectively, to correct the instrument drift. The details of this process were described by Yang et al. (2010) [65].

4. Results

Appendix A Tables A1–A5 show the complete datasets for the zircon U-Pb dating, whole-rock major, trace, rare earth element, Sr-Nd-Pb isotopic ratio, and zircon Lu-Hf isotopic ratio results obtained using the mafic-ultramafic samples from ophiolites in the Sabah area.

4.1. Zircon U–Pb Ages

Nine zircons were selected from peridotite (sample KDS-KET-a). These zircons have euhedral to subhedral columnar shapes, and range in size from 30 to 60 μm, with aspect ratios of about 1.5:1 to 2.5:1, and show zoned sectors or irregular–regular oscillatory zoning in CL images (Figure 4). Th/U ratios of these zircon grains ranged from 0.18 to 1.10, with an average of 0.59. The weighted average $^{206}Pb/^{238}U$ age of the youngest age group is 248.1 ± 4.6 Ma (95% confidence, MSWD = 0.58, $n = 9$) (Figure 5a), which is considered to represent the crystallization age of the peridotite. A couple of spots yield ages of 440.9 Ma and 461.9 Ma. The oldest ages detected are 1946.8 Ma and 1859 Ma.

A total of 25 spot analyses were acquired on sample ND-KET-b, of which 24 were valid. The zircons are mostly short columnar or round in shape and range in size from 50 to 150 μm, with a length–width ratio of 1:1 to 2:1 and Th/U values ranging from 0.43 to 1.01. Oscillatory zoning is not always observed, typical of mafic rocks zircon (Figure 4). The $^{206}Pb/^{238}U$ age of the 24 measured points ranged from 235.1 ± 6.6 to 251.5 ± 11.5 Ma, with a weighted average age of 244.9 ± 3.2 Ma (Figure 5b).

A total of 70 zircons were selected from sample KM-KET-a, obtaining 52 feasible data points. These zircons are mostly short columnar or round in shape, and range in size from 30 to 100 μm, with a length–width ratio of 1:1 to 2:1 and Th/U values ranging from 0.01 to 4.64. Oscillatory zoning is documented in many crystals, indicating the characteristics of magmatic zircons (Figure 4). The $^{206}Pb/^{238}U$ and $^{207}Pb/^{206}Pb$ ages range from 245 ± 6 to 2997 ± 19 Ma, with a weighted average age of 245 ± 6 Ma, showing the characteristics of detrital zircons (Figure 5c,d).

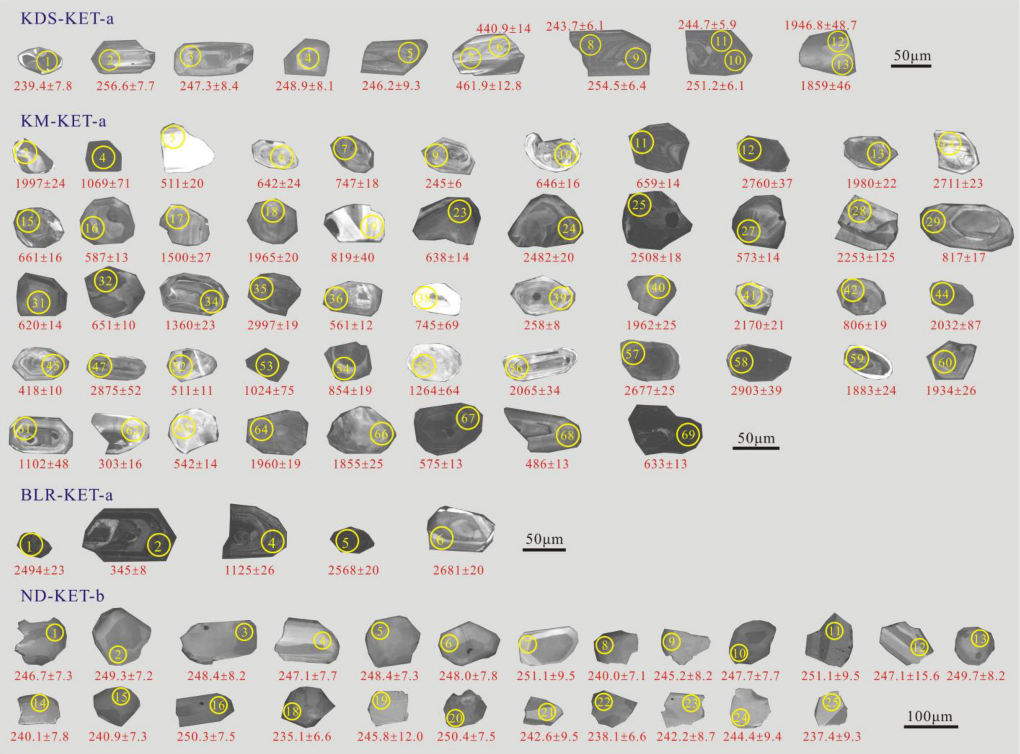

Figure 4. CL images of zircons from the Sabah area samples.

A total of five zircons were selected from the sample BLR-KET-a (Figure 4). These zircons have subhedral shapes and range in size from 50 to 120 μm. Th/U ratios of these zircon grains range from 0.47 to 1.44. The minimum ^{206}Pb/^{238}U age is 345 ± 8 Ma. The ages of the other zircons are 2494 ± 23 Ma, 1125 ± 26 Ma, 2568 ± 20 Ma, and 2681 ± 20 Ma. These zircons are captured zircons.

A total of 83 spot analyses were completed, of which 48 passed the concordance test (sample SP-a). The majority of the zircon grains are euhedral to subhedral in shape, as well as short-columnar, irregular, or stocky. The sizes of the grains range from 50 to 120 μm, with aspect ratios of 1:1–3:1. The colors are gray-black and bright white. The zircon grains are angular to subrounded. In CL, oscillatory structures could be seen, as well as evidence of resorption and later transformation of some zircons. The zircon Th and U contents and Th/U ratios are 36.78–905.03 ppm, 50.86–2115.46 ppm, and 0.08–1.44, with an average of 0.52, respectively. On the base of their internal structure, most of these zircons seem to have magmatic origin. The zircon ages ranged from 81.4 ± 2.0 to 2577.9 ± 35.2 Ma. The age spectrum of zircons of subgroup Sp-a can be divided into six main age clusters as follows: 81.4–127.2 Ma (9%), 170.5–334.4 Ma (27%), 408.5–972.9 Ma (27%), 1097.6–1195.0 Ma (9%), 1329.5–1508.9 Ma (7%), and 1645.4–2577.9 Ma (21%), with the age peaks at 105.4 Ma, 238.0 Ma, 570.5 Ma, 1111.7 Ma, 1353.1 Ma, and 1855.5 Ma, respectively (Figure 5e,f).

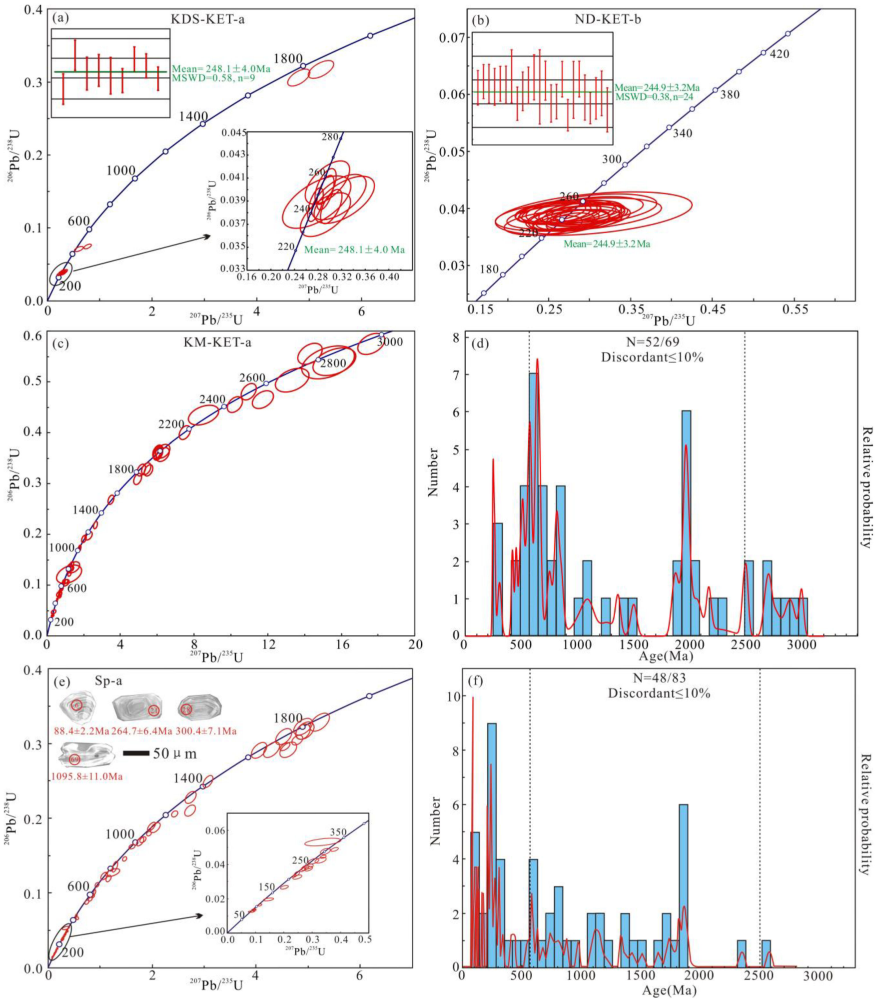

Figure 5. LA-ICP-MS U-Pb concordia diagram, weighted mean age diagram, histogram, and probability density distribution diagram. (**a**) Serpentinite peridotite, KET; (**b**) gabbro, KET; (**c**–**d**) basalt, KET; and (**e**–**f**) sandstone from Sp.

4.2. Zircon Lu-Hf Isotopes

Based on the zircon U-Pb isotope analyses (sample KDS-KET-a, nine zircons), 12 points were selected for zircon Hf isotope analysis. The analysis data are shown in Table A5. The $^{176}Hf/^{177}Hf$ measured at eight zircon grains with Middle Triassic U-Pb ages is 0.282364–0.282940, with an average of 0.282463. The $^{176}Lu/^{177}Hf$ is 0.000995–0.001810, with an average of 0.001242. The zircon $\varepsilon_{Hf}(t)$ ranges from −10.2 to 11.1, the Hf isotope single-stage model age (t_{DM1}) from 451 to 1312 Ma, and the two-stage model age (t_{DM2}) from 566 to 1929 Ma.

4.3. Whole-Rock Major, Trace, and Rare Earth Elements

4.3.1. Mafic Rocks from Ophiolites in the Sabah Area

The basalt and diabase of the northwest, central, and southeast Sabah areas contain SiO_2 concentrations of 49.84–58.94 wt.% (average 52.76 wt.%). The K_2O concentrations of these samples are 0.01–2.19 wt.%, and the Na_2O concentrations are at 2.50–6.11 wt.%. The chondrite-normalized rare earth element (REE) patterns of the BLR-CS basalt and BLR-KET diabase samples show depletion in light (L) REEs. The distribution pattern is similar to that of normal mid-ocean ridge basalt (N-MORB) (Figure 6a,c). The LREE values are 13.73–29.08 ppm (average 22.14 ppm), and the heavy (H) REE values are 12.41–18.79 ppm (average 15.21 ppm). The LREE/HREE values range from 1.02 to 1.69, with $(La/Yb)_N$ values from 0.41 to 0.9. In the primitive mantle-normalized trace element spidergram, these samples show pronounced positive anomalies in U, Ta, Sr, and Hf and negative anomalies in Th, Nb, K, and P (Figure 6b).

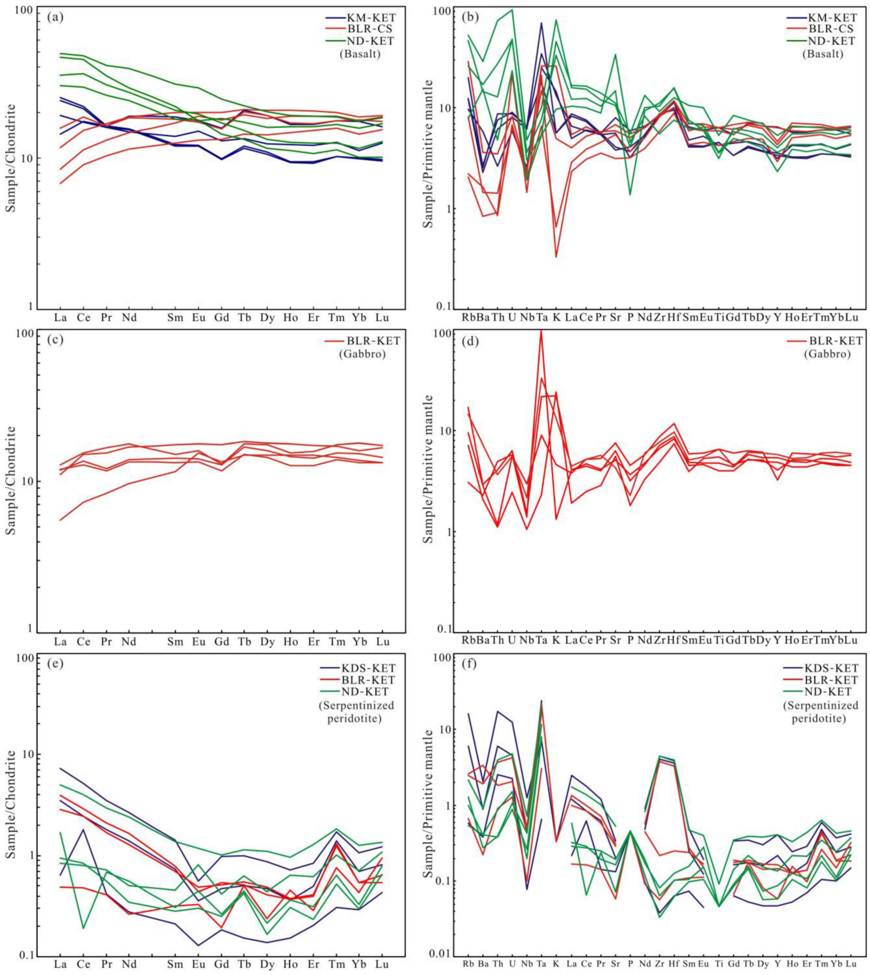

Figure 6. Chondrite-normalized rare earth element abundances (**a**,**c**,**e**) and primitive mantle-normalized trace element abundances (**b**,**d**,**f**) for the igneous rocks of KET and Cs in the Sabah area. The normalizing values are from Sun and McDonough (1989) [66].

The chondrite-normalized REE diagrams of KM-KET and ND-KET basalt samples show LREE enrichment and incline to the right. The distribution is similar to enriched mid-ocean ridge basalt (E-MORB) but with slightly higher elemental contents (Figure 6a). The LREE values are 26.53–68.82 ppm (average 42.03 ppm), and the HREE values are 9.38–19.11 ppm (average 13.18 ppm). The LREE/HREE ratios are from 1.73 to 3.91, with $(La/Yb)_N$ values of 0.83–3.05 (average 2.40). In the primitive mantle-normalized trace element spidergram, these samples show pronounced positive anomalies in U, Ta, K, and Hf and negative anomalies in Ba, Nb, P, Ti, and Y (Figure 6b).

4.3.2. Ultrabasic Rocks from Ophiolites in the Sabah Area

The peridotite contains SiO_2 concentrations of 40.73–47.34 wt.% (average 43.51 wt.%). The K_2O and Na_2O concentrations are very low. The loss on ignition of these samples is 9.84% to 13.59%, and they underwent strong alteration. Primitive mantle-normalized trace element diagrams and chondrite-normalized REE diagrams for these peridotites are shown in Figure 6e. The chondrite-normalized REE patterns show a zigzag pattern with low rare earth element contents. The LREE concentrations range from 0.64 to 6.69 ppm (average 2.73 ppm), and the HREE values from 0.19 to 1.09 ppm (average 0.5 ppm). The LREE/HREE ratios vary between 2.05 and 7.66, and the $(La/Yb)_N$ values vary between

1.12 and 6.79. In the primitive mantle-normalized trace element spidergram, these samples show pronounced positive anomalies in Th, U, Ta, and Tm, negative anomalies in Ba, Nb, and Ti, and K is missing (Figure 6f).

4.4. Sr-Nd-Pb Isotopes

Four samples were analyzed for Sr isotopic compositions (KM-KET-2–3, basalt; BLR-KET-5–6, gabbro), ten for Nd isotopic compositions (KM-KET-2–3, basalt; BLR-KET-4–6, gabbro; KDS-KET-2–3, BLR-KET-2–3, ND-KET-4, serpentinized peridotite), and four for Pb isotopic compositions (KM-KET-2–3, Basalt; BLR-KET-5–6, gabbro). The analysis data are shown in Table A4. The initial Sr, Nd, and Pb isotopic compositions of the samples were calculated using their corresponding zircon U-Pb ages of 248 Ma. The ^{87}Sr/^{86}Sr of the four samples are between 0.70469 and 0.70758, and the initial ratios at 248 Ma are 0.70331–0.70691. The ^{206}Pb/^{204}Pb of the four samples is 16.588–18.442, ^{207}Pb/^{204}Pb is 15.421–15.637, and ^{208}Pb/^{204}Pb is 36.303–38.506. The ^{143}Nd/^{144}Nd of the five basalt and diabase samples is 0.51276–0.51309, the initial (^{143}Nd/^{144}Nd)$_i$ is 0.51251–0.51277, and the ε_{Nd}(t) ranges from 3.66 to 8.73, with an average of 6.33. The two-stage modal age t_{DM2} values range from 308 to 723 Ma, with an average of 504 Ma. The ^{143}Nd/^{144}Nd of the five serpentinized peridotite samples is between 0.51161 and 0.51248, with initial (^{143}Nd/^{144}Nd)$_i$ values ranging from 0.51143 to 0.51230, and the ε_{Nd}(t) from -17.31 to 0.38. Finally, the two-stage modal age t_{DM2} values range from 1051 to 2424 Ma.

5. Discussion

5.1. Origin of the Zircon in the Ophiolites

5.1.1. Studies on Zircon in Ultrabasic Rocks—Basic Rocks

Primitive mantle peridotites have low Zr content and Si activity and theoretically cannot directly crystallize zircon [67]. Consequently, the origin of zircon in peridotites is widely debated. Zircon in ultrabasic rocks is normally thought to have been formed by metasomatic action produced by dehydration in the asthenosphere or subducting lithosphere [68–72], such as metasomatism caused by Si-rich melts or fluids [71]. Zircon in ultrabasic rocks may also be directly captured from crustal materials [72,73]. Shen et al. (2017) summarized previous research on the discovery of zircon in orogenic peridotites [74–78], ophiolite-type ultrabasic rocks [72,73,79], and ultrabasic rocks of mantle xenoliths [74,80].

Orogenic peridotites refer to geological peridotite blocks with metamorphic textures exposed in ultrahigh-pressure collision orogenic belts [81–83]. Zircons in orogenic peridotites are usually interpreted to be the result of metamorphic recrystallization or metasomatism of melts or fluids [74], and metasomatic zircons may record peak metamorphism. The main views on the origin of zircons in orogenic peridotites include mantle fluid metasomatism [74], subduction-related crustal fluid metasomatism [75], injection of granitic magma during peridotite emplacement [79], and subducting crustal fragments [72]. Newly grown and relict zircons have been discovered in peridotites from the Zhimafang [74], Weihai [84], Hujialing [71], Bixiling, and Raobazhai areas of the Sulu–Dabie orogenic belt [83], as well as the Lvliangshan orogenic belt in North Qaidam and the Kokchetav orogenic belt [77,85]. Newly grown zircons are believed to be zircons formed by metasomatism of mantle melts and fluids [74], and relict zircons are believed to be old zircons captured from surrounding rocks during the physical transport of subducting crustal source fluids into peridotite or diagenetic processes [84,86].

Oceanic ophiolite-type ultrabasic rocks are common in ophiolite belts. The zircon ages of the Norbusa ophiolite suite in southern Tibet, Dongqiao ophiolite in Tibet, and oceanic ophiolite-type ultrabasic rocks in the Tumut area of southeastern Australia are widely distributed [72,73,79]. These zircons have the characteristics of crust-derived captured zircons, similar to those of detrital zircons. Robinson et al. (2015) suggested that continental crust materials entered the upper mantle through subduction, while relict materials circulated into newly formed ophiolites, resulting in the presence of zircons in ophiolites [73]. Zircons in ultrabasic rocks of the oceanic ophiolite type may have originated in one of the following ways: zircons obtained from the mixing of overlying continental materials during the diagenetic process of oceanic ophiolites; the cold intrusion of oceanic ophiolite-type ultrabasic rocks, with crustal materials entering ultrabasic rocks; at a certain depth in the subduction zone, the subducting plate fluid carrying zircons into the oceanic ophiolites; or ultrabasic rock serpentinization of some fluids carrying Si and Zr substances, leading to the formation of retrograde metamorphic hydrothermal zircons in ophiolites [78].

Zircons from mantle peridotite xenoliths are mostly zircon xenocrysts scavenged by mixing crustal materials, and their ages correspond to geological events that occurred in the crust [59,80]. For example, the zircons from Xinyang peridotite xenoliths at 210–240 Ma reflect the collision period between the North China Craton and the Yangtze plate [74].

5.1.2. Zircon Age Characteristics and Significance of Sabah Ultrabasic Rocks and Basic Rocks

Zircon selection and analysis were conducted on four samples of basic and ultrabasic rocks from ophiolites in the Sabah area. The nine zircons that were selected from the peridotite sample KDS-KET-a show a wide distribution of ages (239.4 ± 7.8–1946.8 ± 48.7 Ma), and their distribution characteristics are similar to those of detrital zircons. The zircon at point #1 may be metamorphic (Figure 4), while the other eight zircons display metamorphic zoning and characteristics of magmatic zircons. If determined according to the dating method of detrital zircons, the age of peridotite is 239.4 ± 7.8 Ma. However, the zircon morphology represented by 239.4 ± 7.8 Ma is round and unzoned; it may be metamorphic zircon, and Pb elements may be missing [87,88]. Therefore, the average zircon age of the youngest age group, 248.1 ± 4.0 Ma (Figure 5a), was adopted as the age of peridotites. The Middle Proterozoic zircons with ages of 1946.8 ± 48.7 and 1859 ± 46 Ma show some rounding and no recrystallization in morphology. This zircon was captured by peridotite. The Ordovician zircon represented by 440.9 ± 14 and 461.9 ± 12.8 Ma does not show recrystallization either. This zircon was also captured by peridotite.

The 70 zircons that were selected from the basalt sample KM-KET-a also show a wide distribution of ages (245 ± 6–2997 ± 19 Ma), and their distribution characteristics resemble those of detrital zircons. If determined according to the dating method of detrital zircons, the age of basalt is approximately 245 ± 6 Ma. The zircons mainly consist of Proterozoic zircon (71%), followed by Archean zircon (12%) and Cenozoic zircon (17%). The abundance of zircons from the Proterozoic and Archean periods indicated the involvement of paleo-plate materials.

The five zircons from gabbro BLR-KET-a show Archean and Proterozoic, reflecting the involvement of paleo-plate materials.

The 25 zircons from gabbro ND-KET-b display a relatively uniform distribution of ages (235.1 ± 6.6–251.5 ± 11.5 Ma), with an average age of 244.9 ± 3.2 Ma. The oscillatory zones are poorly developed in these zircons, indicating that they may be basic magmatic zircons rather than acidic magmatic zircons. These zircons were formed during crystallization of gabbro itself and suggest the formation of gabbro during the Middle Triassic.

The zircon ages of three samples show age characteristics of detrital zircons (KDS-KET-a, KM-KET-a, and BLR-KET-a), while one shows those of concentrated igneous rocks (ND-KET-b). The ages of rocks fall into the range of 248–244 Ma, while the peridotite is older. Wang et al. (2023) analyzed the age of the basic rocks in the Sabah area. They found that the zircon U-Pb age ranged from 153 to 112 Ma, while the whole rock Ar-Ar age ranged from 184 to 92 Ma, indicating that the basic rocks formed in the Early Jurassic [14]. The reason for the difference in age may lie in the sample locations from the middle–upper part of the ophiolite suite. In addition, there are differences in the trace elements of zircon xenocrysts with different tectonic settings [89]. Thus, zircon trace elements can be used to distinguish the formation environment of host rocks [90–92]. The KDS-KET-a and ND-KET-b samples, along with the collection of zircon trace element data taken from the literature, were plotted on different types of diagrams. In the Ta-Nb, U-Er, Yb-Y, and Lu/Hf-Y diagrams (Figure 7a–d), most of the data points were located in the volcanic arc and intraplate rock regions, while some data points of the sample ND-KET-b were located in the mid-ocean ridge region. In the U/Yb-Y and U/Yb-Hf diagrams, the data points were mostly located within the range of continental zircons (Figure 7e,f), while some data points of the sample ND-KET-b were located near the zircons in the oceanic crust. Based on the age of zircons, the KET ultrabasic rock samples in northwestern Sabah were captured zircons (KDS-KET-a, KM-KET-a, and BLR-KET-a), and their minimum age represented the lower limit of rock formation age. The KET basic rock samples in Southwest Sabah were magmatic crystalline zircons (ND-KET-b), representing the age of rock formation. In summary, the KET ultrabasic rocks and basic rocks at the bottom of the ophiolites may have existed since the Early to Middle Triassic, and paleo-plate materials took part in their formation.

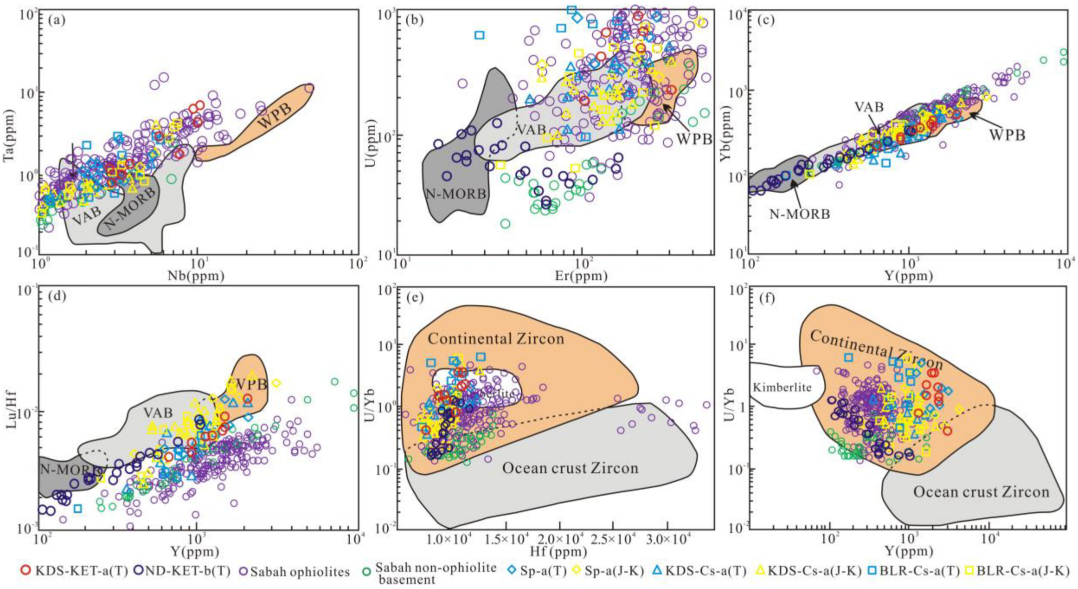

Figure 7. Discrimination diagrams for the tectonic setting of the host rocks of zircon (**a**–**d**), after Schulz et al. (2006) [91]), zircon Hf versus U/Yb and Y versus U/Yb diagrams (**e**,**f**), after Grimes et al. (2007, 2015) [92,93]). Sabah ophiolites and non-ophiolite basement data from Wang et al. (2023) [14]. KDS-Cs-a and BLR-Cs-a data from Tian et al. (2021) [94].

5.2. Basic Rock Source Area and Tectonic Setting of Ophiolites in the Sabah Area

The major elements of the rocks indicate that the ultrabasic rocks in the ophiolites underwent severe alteration, with peridotite transformed into serpentinized peridotite, and the alteration of the basic rocks was relatively weak. The rare earth element distribution diagram of basic rocks shows that those of the ophiolite suite in Northwest and Southeast Sabah are of an E-MORB type (LREE enrichment), while those in Central Sabah are of the N-MORB type (LREE depletion). As shown by the Zr/Nb-La/Yb (Figure 8a), La/Sm-Sm/Yb (Figure 8b), Nb/Yb-Th/Yb (Figure 8c), and Nb/Yb-TiO_2/Yb diagrams (Figure 8d), the basic rocks in Central Sabah are of the N-MORB type, while those in Southeast Sabah are of the E-MORB type. The occurrence of E-MORB in mid-ocean ridges is usually caused by the influence of enriched components on the depleted asthenospheric mantle [95,96]. The enriched sources may have the following origins: hotspots or mantle plumes near ocean ridges [97]; enriched lower mantle [98]; melts generated by the melting of eclogite after subduction of the oceanic crust into the upper mantle [99]; and shallow mantle enrichment caused by oceanic islands or seamounts subducting into the upper mantle [100]. In the tectonic setting discrimination diagram (Figure 8e,f), the ophiolite samples mostly fall into the vicinity of mid-ocean ridges. Compared with the Mesozoic basic rocks of Hainan Island, Palawan Island, Kuching Belt, Southwest Borneo, and Meratus, the Early to Middle Triassic basic rocks of Hainan Island, which have similar ages, were formed in an intracontinental extensional setting [101,102], while the Cretaceous basic rocks of the Kuching Belt, Southwest Borneo, and Meratus were volcanic arc basalt formed under the background of oceanic crust subduction. In the geological context of the subduction of the Paleo-Tethys Ocean plate during the Early Triassic, collision between the South China and Indo-China plates may have formed an extensional setting at the edges of the South China or Indo-China plate, leading to the upwelling of magma and the formation of ophiolites.

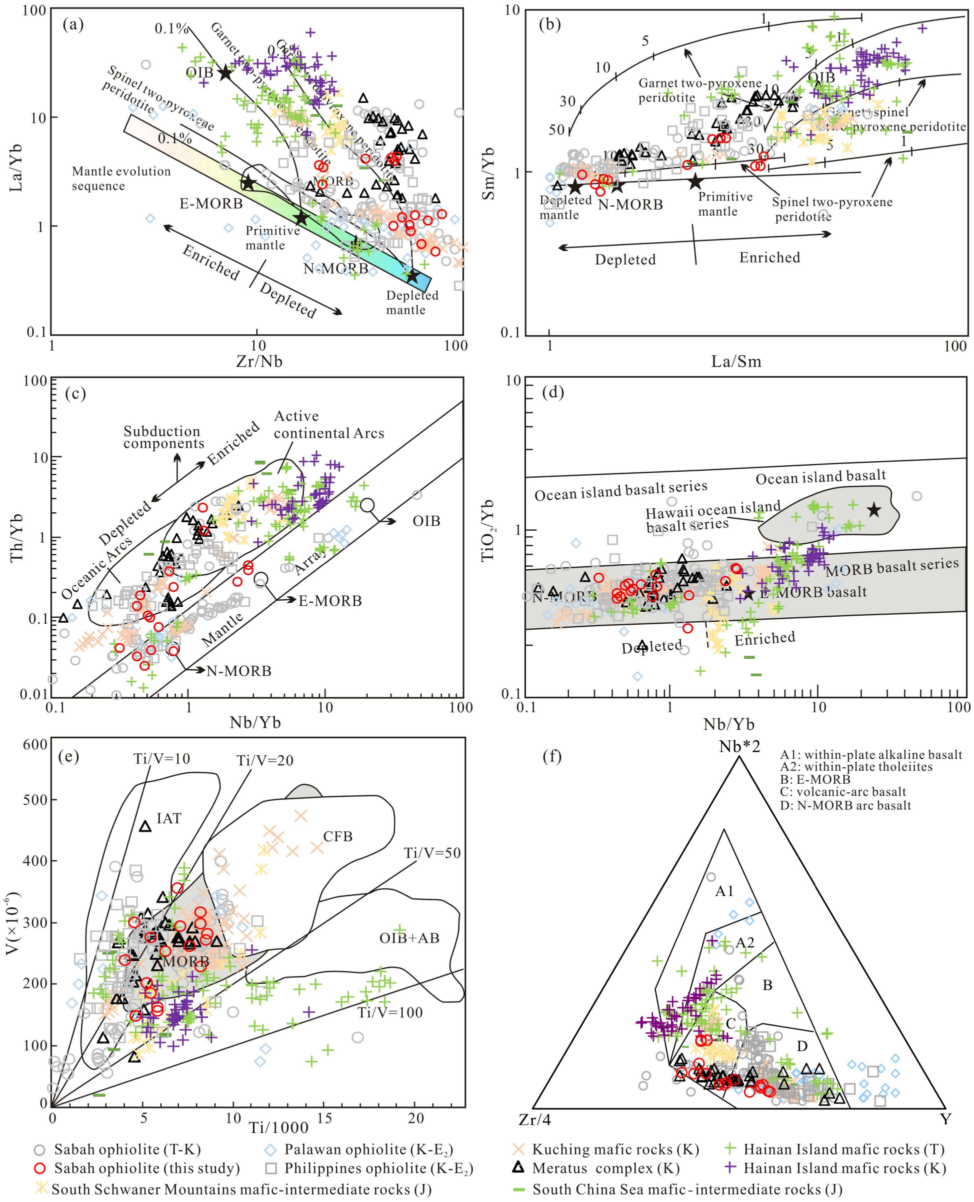

Figure 8. Plots of Zr/Nb versus La/Yb ((**a**), after Göncüoglu et al. (2010) [103]), La/Sm versus Sm/Yb ((**b**), after Pearce et al. (2008) [104]), Nb/Yb versus Th/Yb (**c**), after Pearce et al. (2008) [104]), Nb/Yb versus TiO_2/Yb (**d**), after Pearce et al. (2008) [104]), Ti/1000 versus V (**e**), after Shervais (1982) [105]), and 2Nb versus Zr/4 versus Y (**f**), after Meschede (1986) [106]) for the mafic rocks from the Sabah ophiolites. Sabah ophiolite data from Wang et al. (2023) [14]. Palawan ophiolite data from Gibaga et al. (2020) and Dycoco et al. (2021) [46,47]. Kuching mafic rock data from Wang et al. (2021) [51]. Meratus complex data from Wang et al. (2022) [16]. Philippine ophiolite data from Yumul et al. (2013), Deng et al. (2015), and Guotana et al. (2017) [107–109]. South Schwaner Mountains and South China Sea mafic–intermediate rock data from Wang et al. (2022) [52]. Hainan Island mafic rock data from Tang et al. (2010), Chen et al. (2014), Zhou et al. (2015), Shen et al. (2018), and Liu et al. (2022) [101,102,110–112].

The trace element spidergram shows that the basic rocks are enriched in Ta and Hf and depleted in Nb and Th. The ratios of Nb, Th, Sm, La, Ba, Zr, and other elements can be used to constrain the composition, melting, and mixing degree of the magmatic source. Figure 9 shows that the magmatic source of the Sabah basic rocks is influenced by subduction plate melting and fluid addition. The ε_{Nd}(t) values of basic rocks in ophiolites from the Sabah area ranged from 3.66 to 8.73, similar to those of the basic rocks in Kuching and the Meratus mélange zone and higher than those of the Triassic and Cretaceous basic rocks of Hainan Island (Figure 10a). According to the Pb isotope data, the Sabah basic rocks resemble Meratus ophiolites and tend to have a Pb isotope composition in the Tethys Ocean domain (Figure 10b,c). The influence of time factors can be eliminated, and the source area of lead can be traced through the $\Delta\beta$-$\Delta\gamma$ genetic classification diagram ($\Delta\beta$ and $\Delta\gamma$ are Pb isotope relative deviation values, calculated using the method from [113]). The diagram shows that the Pb isotope data points of the Sabah basic rocks mainly plot into the fields of mantle source lead, orogenic belt lead, and mixed leads of the upper crust and mantle subduction zones (Figure 10d), indicating that the magmatic source may have been affected by subduction plate materials. The ε_{Hf}(t) values of zircons from the ultrabasic rocks in the ophiolite ranged from -10.2 to -6.1, similar to those of the Hainan Island mélange and Triassic granite basement of the Qiongdongnan Basin, with older materials involved in the magmatic source. The relatively high ε_{Hf}(t) values of zircons in the non-ophiolite basement indicate the involvement of younger oceanic crust materials, which differ significantly from the zircons of the ultrabasic rocks in the ophiolites (Figure 11). Wang et al. (2023) classified basic rocks into the following three types: MORB, Nb-enriched, and high-Nb, based on the geochemical differences in Kudat (approximately 135–11 Ma), Telupid (approximately 185–140 Ma), and Darvel Bay (185–85 Ma) ophiolite suite basic rocks in Sabah [14]. The magmatic source was altered by plate-derived melts and formed in the fore-arc setting of Paleo-Pacific plate subduction. Therefore, based on the rock geochemistry and isotope data, it is believed that the basic rocks of the ophiolites in the Sabah area formed in an extensional setting, while the magmatic source was influenced by the melting of subducted plates and fluids in the Paleo-Tethys Ocean.

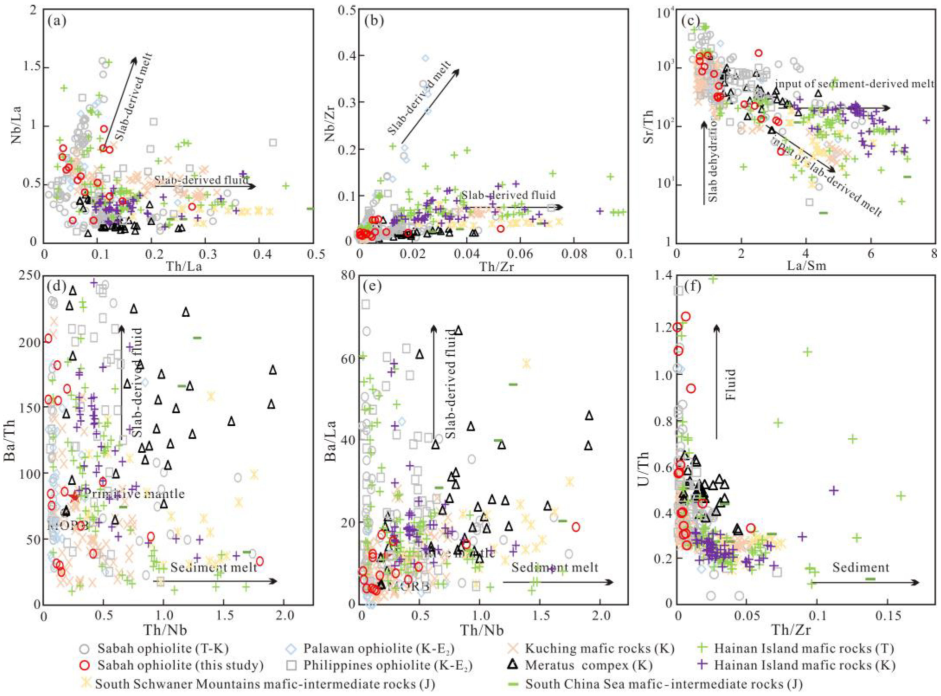

Figure 9. Plots of Th/La versus Nb/La ((**a**), after [14]), Th/Zr versus Nb/Zr ((**b**), after [14]), La/Sm versus Sr/Th ((**c**), after [14]), Th/Nb versus Ba/Th (**d**), after [114]), Th/Nb versus Ba/La ((**e**), after [114]), and Th/Zr versus U/Th ((**f**), after [115]) for the basalt from the Sabah ophiolites.

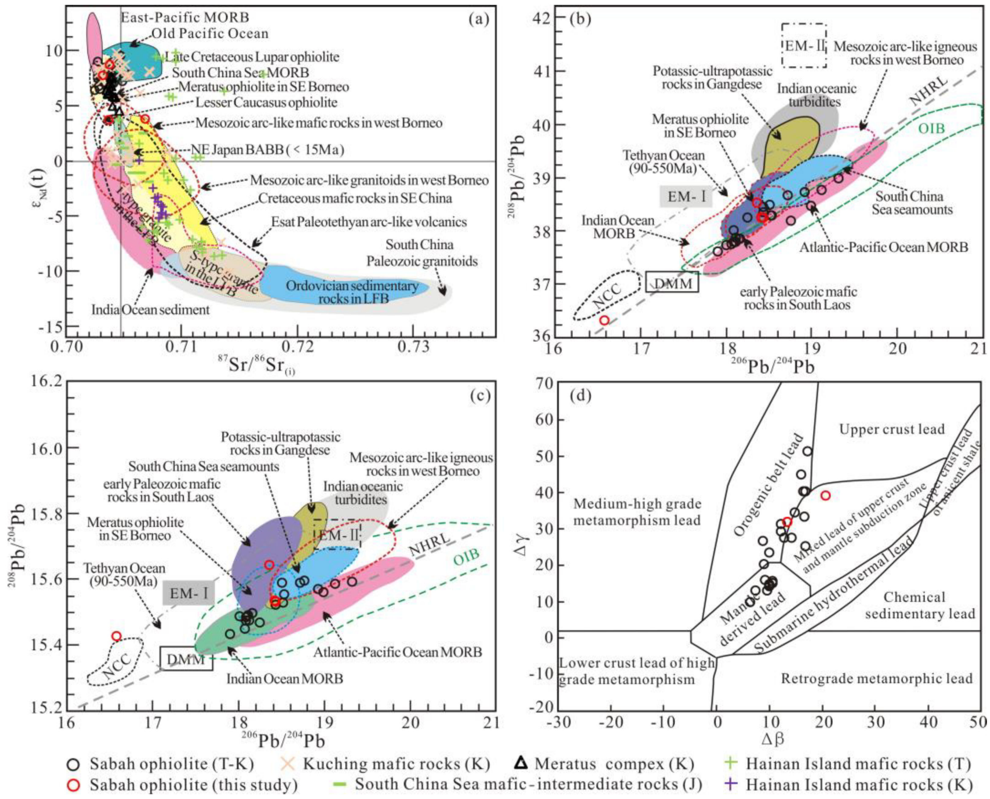

Figure 10. Initial $^{87}Sr/^{86}Sr$ versus $\varepsilon_{Nd}(t)$ (**a**), $^{206}Pb/^{204}Pb$ versus $^{208}Pb/^{204}Pb$ and $^{207}Pb/^{204}Pb$ (**b**–**c**), and Δβ versus Δγ (**d**). NHRL, with a northern hemisphere reference line. Data are from Zindler and Hart (1986), Burton-Johnson et al. (2020), and Wang et al. (2018, 2020, 2021, 2022, 2023) [14,16,19,25,41,53,54,100,116–120].

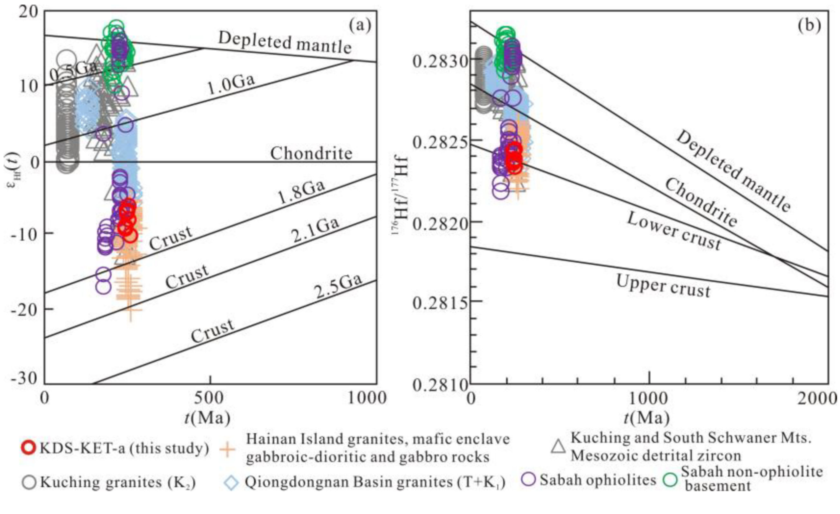

Figure 11. Hf isotopic composition versus age of the zircons from sample KDS-KET-a: (**a**) εHf(*t*)-*t* diagram and (**b**) $^{176}Hf/^{177}Hf$-*t* diagram. The chondrite and depleted mantle lines are from Blichert-Toft and Albarède (1997) and Griffin et al. (2000) [61,62].

5.3. Tectonic Evolution of the Ophiolites in the Sabah Area

The tectonic evolution of Sabah has been discussed previously by many authors [20–23]. Some scholars suggested that the subduction of the South China Sea and Sulu Sea oceanic lithospheres played a significant role in the tectonic evolution of the Sabah area [28,29]. Although many studies have been carried out on the Cenozoic tectonic evolution of Sabah, only a few have been devoted to the pre-Cenozoic. Hutchison (1978) and Tongkul (1991) suggested that the extrusion of basalts and intrusion of ultrabasic rocks tended to occur in older metamorphosed oceanic basements during the Early Mesozoic, and radiolarian cherts tended to be deposited in newly formed oceanic basements [28,29]. Omang and Barber (1996), based on data regarding large ion lithophile elements and high-field strength elements in ophiolites, argued that the ophiolites in the Sabah area were formed in the context of a supra-subduction zone [30]. Sabah and East Kalimantan are not a single block; instead, they drifted and amalgamated together from elsewhere [21]. Sabah was formed by the rupture of the Australian plate [24]. Graves et al. (2000) suggested that the ophiolitic basement of Sabah could be interpreted as having formed as an integral part of either the Western Pacific or the Eastern Indian Oceans [18]. Burton-Johnson et al. (2020) suggested that ophiolites in Southeast Sabah were emplaced in an extensional supra-subduction zone and rifted the continental margin of Sundaland [25]. Wang et al. (2023) concluded that the basic rocks of the ophiolites were formed in the fore-arc setting of the Paleo-Pacific plate subduction [14,19]. There is also some controversy over whether the basement of the Sabah region is continental or oceanic crust. Considering the presence of granite and metamorphic rocks in Southeast Sabah, and combined with gravity data, Leong (1974) speculated that the Sabah area derived from continental crust [17].

The ophiolites in the Sabah area underwent subduction, collision, tectonic superimposition, and reworking between plates, including interference from magmatic activity and varying degrees of metamorphism, such as severe serpentinization of peridotite. First, it is necessary to determine how the ophiolites formed and what type of ophiolites they are. Based on the geochemical characteristics of ophiolites, Dilek and Furnes (2011) classified them into non-subduction-related types, including continental margin (CM) (Figure 12a) [121], mid-ocean-ridge (MOR), plume-type (P), and subduction-related, including supra-subduction zone (SSZ) (Figure 12b) and volcanic arc (VA) (Figure 12c) [7,121], and proposed evolutionary models and simple columnar profiles of ophiolites. The continental margin-type ophiolites were formed in a passive extensional environment of the lithosphere during the expansion stage of the newly formed ocean, such as the current Red Sea and Atlantic margins [122]. Mid-ocean ridge-type ophiolites were formed on mid-ocean ridges either near or far from mantle plumes, mid-ocean ridges near trenches, or back-arc spreading ridges far from trenches [5]. Plume-type ophiolites were formed on the spreading ridge near a mantle plume. Supra-subduction zone-type ophiolites in the subduction zone were formed by the extension of the upper plate after the initial subduction and subsequent rapid retreating [123,124]. Magmas produced MORB-like units and were strongly influenced by processes of plate dehydration and metasomatism, such as the trench–arc–basin system in the west Pacific Ocean margins of the Mesozoic. Volcanic arc-type ophiolites were formed in a simatic arc setting [121]. With the continuous subduction and infiltration of arc magma, the hydrated basic crust partially melted to form tonalite magma, and the relict basic crust transformed into peridotite restite. According to the geochemical characteristics of ophiolites and basement rocks [14,25], ophiolites in the Sabah area do not fall into either the mid-ocean ridge or plume types. From the analysis of rock sequence assemblages, the ophiolites in Northwest and Central Sabah resemble the continental margin type, while those in Southeast Sabah are of the supra-subduction zone type, indicating that the ophiolites may have formed in an extensional environment. Moreover, the emplacement patterns of ophiolites can be roughly divided into fore-arc ophiolites that are easy to emplace, back-arc ophiolites that are difficult to emplace, and mid-ocean ridge ophiolites that are almost impossible to emplace (Figure 12d) [2]. From the perspective of geotectonic settings, the Mesozoic Southeast Asian region was mainly dominated by the subduction zones of the Paleo-Tethys Ocean and the Paleo-Pacific, while the ophiolites in the Sabah area are easily emplaced fore-arc ophiolites.

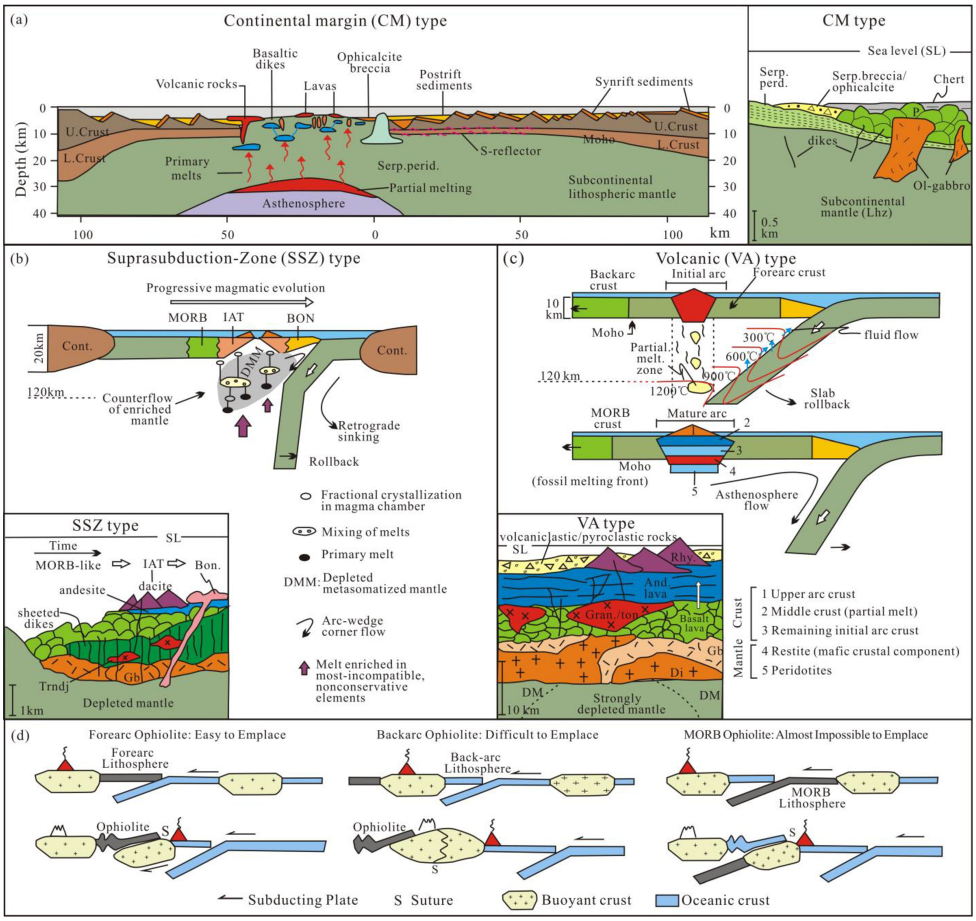

Figure 12. Tectonic settings and processes of continental margin (**a**), supra-subduction zone (**b**), and volcanic (**c**) ophiolite types, with columnar sections depicting the simplified structural architecture of the ophiolite type [121]. Emplacement pattern of ophiolites (**d**) [2].

The zircon U-Pb ages indicate that the ultrabasic rocks in the ophiolites formed during the Early Triassic. Wang et al. (2023), using whole-rock $^{40}Ar/^{39}Ar$ dating for basalts, determined the formation time to be Early Jurassic [14]. The tectonic evolution of Southeast Asia during the Early Triassic was marked by intense subduction of the Paleo-Tethys Ocean plate. The Late Permian–Early Triassic granite and diabase of Hainan Island are products of the subduction and retreating of the Paleo-Pacific plate. Such products are formed in a tectonic environment where the continental island arc transitions from compression to extension and is influenced by the subducting plate of the Paleo-Tethys Ocean, resulting in the retreating of the Paleo-Pacific plate [112]. The geochemical data of the basic rocks in the ophiolites indicate that the magmatic source was influenced by plate subduction. Zircon Lu-Hf isotopes suggest the addition of ancient materials, while the Sr-Nd-Pb isotope data tend toward the conclusion of Tethys Ocean subduction. Therefore, in the Early Triassic, the Paleo-Tethys Ocean plate subducted, and the Paleo-Pacific plate started, forming a relatively small extensional environment near South China or Sundaland, resulting in ophiolites being formed by the upwelling and emplacement of mantle materials (Figure 13a). During the Middle to Late Triassic, the Paleo-Tethys Ocean plate closed, and the subduction of the Paleo-Pacific plate began. The Middle to Late Triassic volcanic island arc granites were developed in South China, Hainan Island [125], Vietnam [126], Malaya, West Borneo [36,41], and Southeast Sabah [25]. From the Jurassic to the Early Cretaceous, the Paleo-Pacific plate was subducted strongly, and volcanic island arc granites were developed in Guangdong, Hainan, the Pearl River Mouth Basin, and the Dangerous Grounds. At that time, ophiolites in the Sabah area, as fore-arc ophiolites, may have been emplaced on the continental crust basement (Figure 13b). In the Late Cretaceous, the age characteristics of detrital zircons in the Cs and Sp sandstone formations resembled those in northeastern Vietnam and the continental margin of South China [94]. The discrimination diagram for the tectonic setting of detrital zircons shows that Cs and Sp were likely deposited in a collision environment (Figure 14). The Cretaceous–Eocene sedimentary rocks of the Dangerous Grounds and Palawan Island mainly originate from the continental margin of South China [127–131]. Therefore, it is speculated that the Cs and Sp formations of the ophiolites originated from the South China or Indochina blocks, indicating that Sabah and Palawan may have been located on the margin of the Dangerous Grounds or Sundaland in the early stage of the Late Cretaceous.

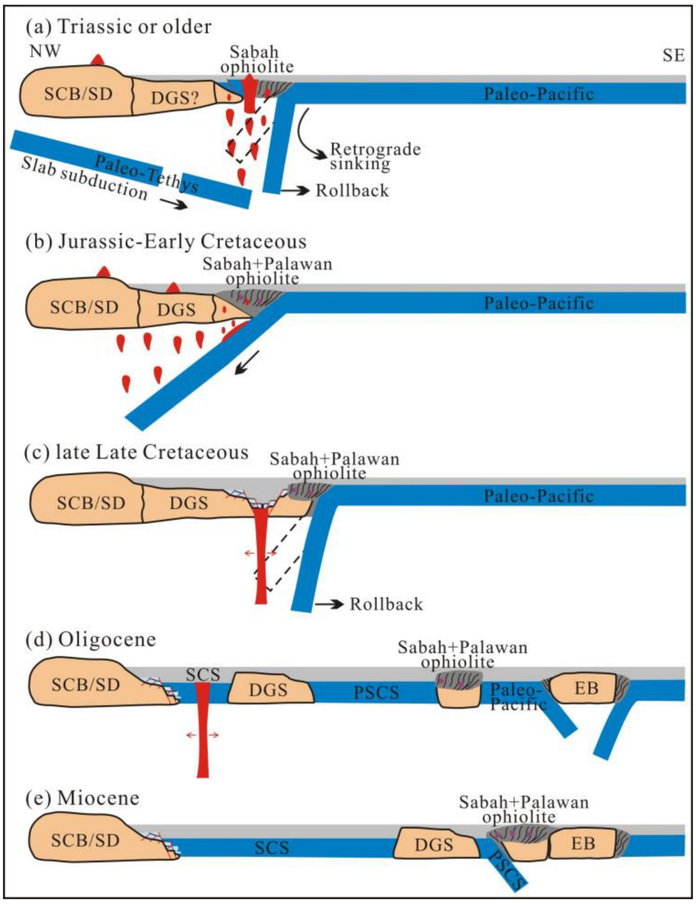

Figure 13. Tectonic cartoons showing the evolution of the Sabah ophiolite. (**a**) In the Triassic or older Sabah ophiolite formed. (**b**) The Jurassic -Early Cretaceous, Sabah ophiolite emplaced on the continental crust basement. (**c**) The late Late Cretaceous, Sabah and Palawan ophiolites split and drifted southward from the margin of the Dangerous Grounds or Sundaland. (**d**) The Oligocene, the suturing of the Sabah and Palawan ophiolites with East Borneo. (**e**) The Miocene, the Sabah orogeny leading to ophiolite exposure. DGS, Dangerous Grounds; EB, East Borneo; PSCS, Proto-South China Sea; SCB, South China Block; SCS, South China Sea; SD, Sundaland.

In the late stage of the Late Cretaceous, the Paleo-Pacific plate subducted and retreated, and the South China Sea changed from a compression environment to an expansion environment [132]. Next, the Proto-South China Sea crust formed and expanded, while the Sabah and Palawan ophiolites split and drifted southward from the margin of the Dangerous Grounds or Sundaland (Figure 13c). The Semitau block in West Borneo was located on the margin of the Sundaland during the Jurassic–Early Cretaceous period; then, along with the expansion of the Proto-South China Sea during the late stage of the Late Cretaceous to Early Eocene, it split from the margin of the Sundaland and sutured with West Borneo [10,11]. In the Oligocene, the South China Sea ocean basin expanded, the

Dangerous Grounds plate split from the northern part of the South China Sea, and Borneo underwent counterclockwise rotation under the influence of the Australian Plate in the south [38], further accelerating the suturing of the Sabah and Palawan ophiolites with East Borneo (Figure 13d). In the Miocene, Sabah had already sutured with East Borneo, and the Dangerous Grounds plate collided with Borneo, causing an uplift (the Sabah orogeny) between Sabah and South Palawan, in turn leading to ophiolite exposure (Figure 13e).

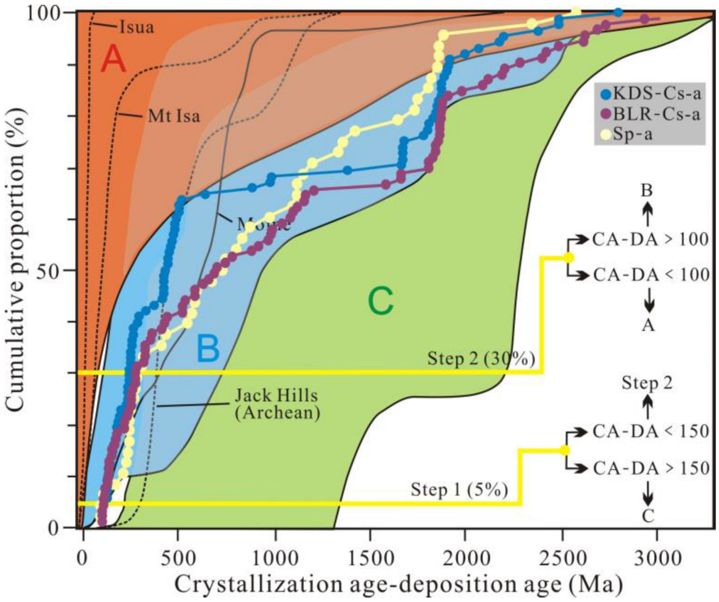

Figure 14. Detrital zircon discrimination diagram (Cawood et al., 2012) [133]. A, convergent settings; B, collisional settings; C, extensional settings. CA, crystallization age; DA, deposition age. The KDS-Cs-a and BLR-Cs-a detrital zircon age data from Tian et al. (2021) [94].

6. Conclusions

The zircon U-Pb ages of ultrabasic and basic rocks in ophiolites in the Sabah area ranged from 248 to 244 Ma, indicating the presence of ophiolites in the Early Triassic. The geochemical characteristics of the basic rocks in the Central Sabah ophiolite are N-MORB-like, while those in Northwest and Southeast Sabah are E-MORB-like. The magmatic source is influenced by the melting of and fluids derived from the Paleo-Tethys subducting plate. The tectonic evolution of Sabah can be traced back to the Early Triassic. At that time, the fast subduction of the Paleo-Tethys Ocean plate and the retreating of the Paleo-Pacific plate resulted in the upwelling of mantle material in relatively small extensional settings, forming the ophiolites. During the Jurassic to Early Cretaceous, the Paleo-Pacific plate was intensely subducted, and ophiolites in the Sabah area intruded into the continental crust of South China or the Sundaland margin as fore-arc ophiolites. During the late stage of the Late Cretaceous to Miocene, ophiolites in the Sabah area, influenced by the expansion of the Proto-South China Sea and South China Sea oceanic crust, drifted southward with microplate fragments and then sutured with East Borneo.

Author Contributions: Writing—original draft preparation, Z.T.; methodology, Y.G.; investigation and resources, P.W.; writing—review and editing, H.T. All authors have read and agreed to the published version of the manuscript.

Funding: This study was supported by the National Science and Technology Major Project (2016ZX05026-004-001), the National Key R&D Program of China (grant No. 2019YFC0605402), and the Major Program of the National Natural Science Foundation of China (grant No. 41790453).

Data Availability Statement: Data is provided in the Appendix A.

Conflicts of Interest: The authors declare no conflict of interest.

Appendix A

Table A1. Zircon U-Pb dating results from the Sabah ophiolites.

Sample	Spot	Th (ppm)	U (ppm)	Th/U	Isotope						Age (Ma)					
					^{207}Pb/^{206}Pb	1σ	^{207}Pb/^{235}U	1σ	^{206}Pb/^{238}U	1σ	^{207}Pb/^{206}Pb	1σ	^{207}Pb/^{235}U	1σ	^{206}Pb/^{238}U	1σ
KDS-KET-a	1	246.89	383.36	0.64	0.05610	0.00543	0.29262	0.02794	0.03783	0.00125	455.8	201.8	260.6	22	239.4	7.8
	2	168.73	235.52	0.72	0.05284	0.00444	0.29593	0.0247	0.04061	0.00124	322.1	179.9	263.2	19.4	256.6	7.7
	3	68.28	175.88	0.39	0.06022	0.00635	0.32473	0.03371	0.03911	0.00135	611.3	212.7	285.5	25.8	247.3	8.4
	4	135.86	233.65	0.58	0.05809	0.00568	0.31529	0.03043	0.03936	0.0013	532.8	201.3	278.3	23.5	248.9	8.1
	5	408.6	620.23	0.66	0.05177	0.00722	0.27788	0.03816	0.03892	0.0015	275.3	291.5	249	30.3	246.2	9.3
	6	90.04	93.41	0.96	0.06173	0.00584	0.60256	0.05639	0.07079	0.00232	664.7	190.5	478.9	35.7	440.9	14
	7	67.09	84.28	0.8	0.07523	0.00456	0.77054	0.04675	0.07428	0.00214	1074.6	117.1	580.1	26.8	461.9	12.8
	8	202.85	876.15	0.23	0.05691	0.00215	0.30239	0.012	0.03853	0.00098	487.5	82	268.3	9.4	243.7	6.1
	9	157.59	633.21	0.25	0.05273	0.00204	0.29280	0.0119	0.04027	0.00103	317	85.9	260.8	9.3	254.5	6.4
	10	225.01	1262.52	0.18	0.05338	0.0016	0.29251	0.00957	0.03974	0.00099	344.9	66.4	260.5	7.5	251.2	6.1
	11	277.54	1372.3	0.2	0.05168	0.00148	0.27564	0.00871	0.03868	0.00096	271.2	64.3	247.2	6.9	244.7	5.9
	12	167.74	163.44	1.03	0.11937	0.00331	5.22537	0.16069	0.31746	0.00808	1946.8	48.7	1856.8	26.2	1777.3	39.5
	13	303.83	276.51	1.1	0.11367	0.00294	4.80168	0.14016	0.30633	0.00768	1859	46	1785.2	24.5	1722.6	37.9
KM-KET-a	2	135.35	218.19	0.62	0.12281	0.00350	5.52551	0.16151	0.32631	0.00751	1997	24	1905	25	1820	37
	4	181.01	1438.31	0.13	0.07501	0.00259	1.78986	0.04838	0.17305	0.00370	1069	71	1042	18	1029	20
	5	30.75	44.00	0.70	0.05992	0.00862	0.68210	0.09624	0.08255	0.00332	601	240	528	58	511	20
	6	0.37	52.43	0.01	0.06933	0.00880	1.00111	0.12421	0.10472	0.00419	909	192	704	63	642	24
	7	318.59	395.79	0.80	0.07295	0.00375	1.23600	0.06292	0.12288	0.00312	1013	63	817	29	747	18
	9	211.03	461.44	0.46	0.05409	0.00519	0.28950	0.02674	0.03882	0.00099	375	220	258	21	245	6
	10	251.03	722.58	0.35	0.06307	0.00373	0.91626	0.05355	0.10536	0.00272	711	80	660	28	646	16
	11	75.43	421.18	0.18	0.06219	0.00311	0.92333	0.04102	0.10767	0.00245	681	109	664	22	659	14
	12	510.68	481.56	1.06	0.19206	0.00858	13.34414	0.60289	0.50391	0.01552	2760	37	2704	43	2631	67
	13	153.83	152.93	1.01	0.12159	0.00316	6.02900	0.16288	0.35963	0.00811	1980	22	1980	24	1980	38
	14	58.94	40.81	1.44	0.18642	0.00542	14.29690	0.43144	0.55623	0.01358	2711	23	2770	29	2851	56
	15	568.60	586.63	0.97	0.06927	0.00391	1.03062	0.05747	0.10792	0.00280	907	72	719	29	661	16
	16	47.00	544.26	0.09	0.05972	0.00197	0.78527	0.02634	0.09537	0.00214	593	37	588	15	587	13
	17	55.14	188.75	0.29	0.09362	0.00275	3.46967	0.10451	0.26880	0.00612	1500	27	1520	24	1535	31
	18	323.99	317.62	1.02	0.12059	0.00289	6.01793	0.15115	0.36195	0.00801	1965	20	1978	22	1991	38
	19	97.83	69.43	1.41	0.07610	0.01266	1.42118	0.23079	0.13546	0.00709	1098	246	898	97	819	40
	23	240.42	295.53	0.81	0.06202	0.00249	0.88957	0.03581	0.10403	0.00242	675	48	646	19	638	14
	24	70.84	133.38	0.53	0.16251	0.00417	10.21047	0.27349	0.45570	0.01044	2482	20	2454	25	2421	46
	25	75.00	260.27	0.29	0.16509	0.00379	10.96148	0.26623	0.48159	0.01069	2508	18	2520	23	2534	47
	27	207.71	282.88	0.73	0.05917	0.00341	0.75843	0.04344	0.09298	0.00233	573	81	573	25	573	14
KM-KET-a	28	173.49	157.80	1.10	0.14214	0.01000	8.52064	0.54573	0.43477	0.01262	2253	125	2288	58	2327	57
	29	138.72	392.65	0.35	0.07312	0.00234	1.36243	0.04426	0.13516	0.00306	1017	32	873	19	817	17
	31	205.25	234.84	0.87	0.06189	0.00263	0.86111	0.03664	0.10091	0.00238	670	52	631	20	620	14
	32	368.24	579.43	0.64	0.05749	0.00216	0.57499	0.02175	0.07254	0.00166	510	45	461	14	451	10

Table A1. *Cont.*

Sample	Spot	Th (ppm)	U (ppm)	Th/U	Isotope						Age (Ma)					
					^{207}Pb/^{206}Pb	1σ	^{207}Pb/^{235}U	1σ	^{206}Pb/^{238}U	1σ	^{207}Pb/^{206}Pb	1σ	^{207}Pb/^{235}U	1σ	^{206}Pb/^{238}U	1σ
KM-KET-a	34	64.00	405.91	0.16	0.08698	0.00225	2.62470	0.07070	0.21886	0.00486	1360	23	1308	20	1276	26
	35	458.55	378.01	1.21	0.22226	0.00571	17.62385	0.47552	0.57516	0.01354	2997	19	2969	26	2929	55
	36	28.37	632.51	0.04	0.06031	0.00236	0.75566	0.02447	0.09088	0.00199	615	86	572	14	561	12
	38	8.53	32.56	0.26	0.07185	0.02701	1.21306	0.44661	0.12247	0.01200	982	603	807	205	745	69
	39	309.30	389.71	0.79	0.05456	0.00963	0.30761	0.05351	0.04089	0.00121	394	367	272	42	258	8
	40	111.53	138.25	0.81	0.12041	0.00352	6.03069	0.18153	0.36330	0.00846	1962	25	1980	26	1998	40
	41	157.38	218.21	0.72	0.13547	0.00342	7.47967	0.19753	0.40048	0.00904	2170	21	2171	24	2171	42
	42	271.39	440.80	0.62	0.07499	0.00343	1.37662	0.06272	0.13315	0.00328	1068	53	879	27	806	19
	44	125.03	200.95	0.62	0.12523	0.00600	6.29223	0.26014	0.36442	0.00883	2032	87	2017	36	2003	42
	45	251.98	486.24	0.52	0.05595	0.00442	0.51700	0.03872	0.06701	0.00167	451	181	423	26	418	10
	47	1286.37	277.18	4.64	0.20571	0.01259	15.28262	0.94343	0.53889	0.02130	2872	52	2833	59	2779	89
	52	16.43	386.96	0.04	0.05915	0.00303	0.67333	0.03077	0.08256	0.00192	573	114	523	19	511	11
	53	182.22	1459.25	0.12	0.07338	0.00266	1.73425	0.05030	0.17142	0.00372	1024	75	1021	19	1020	20
	54	97.07	400.74	0.24	0.06842	0.00411	1.33706	0.07343	0.14173	0.00345	881	128	862	32	854	19
	55	22.34	63.29	0.35	0.08279	0.00446	2.26035	0.12098	0.19805	0.00523	1264	64	1200	38	1165	28
	56	230.36	190.84	1.21	0.12758	0.00486	6.29641	0.24237	0.35800	0.00917	2065	34	2018	34	1973	44
KM-KET-a	57	93.83	198.01	0.47	0.18268	0.00572	11.73159	0.37801	0.46583	0.01165	2677	25	2583	30	2465	51
	58	137.00	176.26	0.78	0.20964	0.01006	15.61993	0.76105	0.54046	0.01796	2903	39	2854	46	2785	75
	59	358.90	274.26	1.31	0.11519	0.00324	4.91603	0.14295	0.30958	0.00711	1883	24	1805	25	1739	35
	60	214.85	110.25	1.95	0.11853	0.00352	5.39592	0.16504	0.33021	0.00771	1934	26	1884	26	1839	37
	61	171.00	215.88	0.79	0.07627	0.00325	2.01255	0.08605	0.19140	0.00468	1102	48	1120	29	1129	25
	62	67.08	132.87	0.50	0.05628	0.01311	0.37382	0.08542	0.04818	0.00264	463	380	322	63	303	16
	63	29.42	111.60	0.26	0.05880	0.00447	0.71082	0.05339	0.08769	0.00241	560	116	545	32	542	14
	64	330.93	778.24	0.43	0.12027	0.00268	5.98053	0.14227	0.36070	0.00792	1960	19	1973	21	1985	38
	66	129.97	225.95	0.58	0.11344	0.00333	5.12062	0.15496	0.32742	0.00760	1855	25	1840	26	1826	37
	67	70.50	236.12	0.30	0.06307	0.00300	0.81075	0.03852	0.09325	0.00226	711	60	603	22	575	13
	68	499.37	444.64	1.12	0.06386	0.00458	0.68927	0.04859	0.07829	0.00219	737	102	532	29	486	13
	69	5.51	1324.97	0.00	0.06165	0.00166	0.87738	0.02458	0.10324	0.00229	662	28	640	13	633	13
BLR-KET-a	1	544.65	1146.64	0.47	0.16366	0.00482	9.44065	0.28508	0.41832	0.01001	2494	23	2382	28	2253	45
	2	0.03	0.02	1.30	0.05325	0.00449	0.40399	0.03265	0.05502	0.00132	339	194	345	24	345	8
	3	196.00	285.43	0.69	0.07713	0.00215	1.84756	0.05287	0.17371	0.00386	1125	26	1063	19	1033	21
	4	577.16	700.71	0.82	0.17107	0.00435	10.67251	0.28260	0.45244	0.01034	2568	20	2495	25	2406	46
	5	67.17	46.62	1.44	0.18305	0.00478	12.14513	0.32942	0.48118	0.01116	2681	20	2616	25	2532	49
ND-KET-b	1	44.28	102.21	0.43	0.05547	0.00504	0.29833	0.02684	0.03901	0.00117	431.1	190.8	265.1	21.0	246.7	7.3
	2	32.66	61.31	0.53	0.04683	0.00491	0.25448	0.02653	0.03942	0.00116	40.2	233.4	230.2	21.5	249.3	7.2
	3	60.07	74.83	0.80	0.04794	0.00614	0.25969	0.0329	0.03929	0.00132	95.4	278.9	234.4	26.5	248.4	8.2
	4	37.72	43.63	0.86	0.04889	0.00623	0.26333	0.03332	0.03907	0.00125	142.3	274.6	237.3	26.8	247.1	7.7
	5	43.95	77.43	0.57	0.05597	0.00492	0.3031	0.02639	0.03928	0.00117	450.8	184.5	268.8	20.6	248.4	7.3
	6	31.28	52.3	0.60	0.05278	0.00584	0.28537	0.03126	0.03922	0.00126	319.3	233.9	254.9	24.7	248.0	7.8
	7	33.61	40.05	0.84	0.05503	0.00982	0.30181	0.0529	0.03978	0.0018	413.5	356.2	267.8	41.3	251.5	11.2

Table A1. *Cont.*

Sample	Spot	Th (ppm)	U (ppm)	Th/U	Isotope						Age (Ma)					
					^{207}Pb/^{206}Pb	1σ	^{207}Pb/^{235}U	1σ	^{206}Pb/^{238}U	1σ	^{207}Pb/^{206}Pb	1σ	^{207}Pb/^{235}U	1σ	^{206}Pb/^{238}U	1σ
ND-KET-b	8	26.72	56.62	0.47	0.05222	0.00492	0.27308	0.02555	0.03793	0.00113	295.1	201.5	245.2	20.4	240.0	7.1
	9	19.62	43.69	0.45	0.05507	0.00654	0.29433	0.03449	0.03877	0.00131	414.9	245.6	262.0	27.1	245.2	8.2
	10	35.16	79.97	0.44	0.04799	0.00525	0.25922	0.02808	0.03918	0.00124	97.8	241.4	234.0	22.6	247.7	7.7
	11	50.16	49.83	1.01	0.05456	0.00821	0.29877	0.04427	0.03972	0.00153	394.4	306.1	265.4	34.6	251.1	9.5
	12	28.95	37.75	0.77	0.05664	0.01505	0.30509	0.07935	0.03907	0.00252	476.7	500.5	270.4	61.7	247.1	15.6
	13	30.2	48.07	0.63	0.0479	0.00639	0.26077	0.03449	0.03949	0.00132	93.1	289.9	235.3	27.8	249.7	8.2
	14	26.51	44.22	0.60	0.05449	0.00693	0.28508	0.03592	0.03795	0.00126	391.5	262.8	254.7	28.4	240.1	7.8
	15	38.86	71.64	0.54	0.05434	0.00495	0.28523	0.02567	0.03808	0.00117	385.0	192.6	254.8	20.3	240.9	7.3
	16	33.59	65.06	0.52	0.0544	0.00525	0.29688	0.0284	0.03959	0.0012	387.5	203.4	264.0	22.2	250.3	7.5
	18	42.24	96.02	0.44	0.05077	0.00398	0.26001	0.02027	0.03715	0.00106	230.5	171.7	234.7	16.3	235.1	6.6
	19	18.62	27.09	0.69	0.05346	0.01271	0.2865	0.06717	0.03887	0.00193	348.3	463.4	255.8	53.0	245.8	12.0
	20	34.97	71.06	0.49	0.05284	0.00503	0.28849	0.02721	0.0396	0.00121	321.9	202.8	257.4	21.4	250.4	7.5
	21	32.62	46.99	0.69	0.05409	0.00813	0.28604	0.04225	0.03836	0.00153	374.7	306.9	255.4	33.4	242.6	9.5
	22	51.73	117.7	0.44	0.05328	0.00376	0.2764	0.01942	0.03763	0.00106	340.5	151.9	247.8	15.5	238.1	6.6
	23	53.41	60.88	0.88	0.05332	0.00709	0.28145	0.03686	0.03829	0.0014	342.2	276.0	251.8	29.2	242.2	8.7
	24	16.51	25.65	0.64	0.05088	0.00907	0.27103	0.04776	0.03863	0.00151	235.6	366.3	243.5	38.2	244.4	9.4
	25	16.83	32.55	0.52	0.05033	0.00838	0.26026	0.04274	0.03751	0.00149	210.1	346.1	234.9	34.4	237.4	9.3
Sp-a	3	36.78	106.41	0.35	0.17207	0.00367	11.34701	0.27522	0.47826	0.01124	2577.9	35.2	2552.1	22.6	2519.7	49.0
	4	905.03	820.29	1.10	0.05111	0.00188	0.11621	0.00442	0.01649	0.00040	245.7	82.6	111.6	4.0	105.4	2.5
	5	149.06	179.19	0.83	0.06179	0.00198	0.74735	0.02519	0.08772	0.00211	666.9	67.3	566.7	14.6	542.0	12.5
	6	367.88	358.74	1.03	0.04939	0.00268	0.09408	0.00514	0.01381	0.00035	166.5	122.2	91.3	4.8	88.4	2.2
	7	346.16	880.45	0.39	0.05217	0.00131	0.26753	0.00737	0.03719	0.00087	293.0	56.3	240.7	5.9	235.4	5.4
	9	102.74	208.65	0.49	0.11037	0.00235	4.90518	0.11902	0.32230	0.00756	1805.5	38.2	1803.1	20.5	1801.0	36.8
	10	89.98	95.24	0.94	0.07992	0.00224	2.06633	0.06222	0.18750	0.00451	1195.0	54.4	1137.7	20.6	1107.8	24.5
	11	117.03	195.55	0.60	0.06356	0.00178	0.81096	0.02441	0.09253	0.00221	727.1	58.3	603.0	13.7	570.5	13.0
	12	469.53	616.46	0.76	0.05533	0.00176	0.28697	0.00963	0.03761	0.00090	425.4	69.2	256.2	7.6	238.0	5.6
	14	59.41	505.74	0.12	0.11390	0.00234	4.94724	0.11737	0.31499	0.00739	1862.5	36.6	1810.4	20.0	1765.2	36.2
	16	261.27	708.97	0.37	0.08978	0.00184	3.07393	0.07296	0.24829	0.00583	1420.8	38.6	1426.2	18.2	1429.6	30.1
	17	120.55	347.80	0.35	0.07081	0.00167	1.16492	0.03073	0.11930	0.00283	951.9	47.7	784.3	14.4	726.6	16.3
	19	175.29	329.91	0.53	0.10617	0.00222	4.52742	0.10912	0.30925	0.00729	1734.6	37.8	1736.0	20.0	1737.0	35.9
	20	257.34	286.23	0.90	0.05454	0.00244	0.20157	0.00917	0.02680	0.00067	393.5	96.6	186.5	7.8	170.5	4.2
	21	101.71	198.76	0.51	0.05263	0.00211	0.30425	0.01256	0.04192	0.00104	312.9	88.8	269.7	9.8	264.7	6.4
	22	295.25	404.24	0.73	0.05202	0.00241	0.09608	0.00453	0.01339	0.00034	286.4	102.7	93.2	4.2	85.8	2.1
	27	193.75	960.37	0.20	0.06171	0.00131	0.93504	0.02297	0.10988	0.00260	664.0	45.0	670.3	12.1	672.1	15.1
	28	150.79	226.46	0.67	0.05271	0.00169	0.34674	0.01178	0.04770	0.00116	316.4	71.3	302.3	8.9	300.4	7.1
	30	56.80	273.42	0.21	0.07685	0.00171	1.99465	0.05057	0.18822	0.00449	1117.3	43.7	1113.7	17.2	1111.7	24.4
	31	82.04	74.70	1.10	0.06406	0.00234	1.08076	0.04116	0.12235	0.00306	743.6	75.5	744.0	20.1	744.1	17.6
	32	118.11	324.42	0.36	0.05203	0.00172	0.27463	0.00957	0.03828	0.00094	286.7	73.6	246.4	7.6	242.1	5.8
	33	181.62	366.07	0.50	0.05362	0.00194	0.28760	0.01086	0.03890	0.00096	354.9	79.6	256.7	8.6	246.0	6.0
	34	84.32	229.97	0.37	0.10115	0.00211	4.05454	0.09859	0.29069	0.00694	1645.4	38.2	1645.2	19.8	1645.0	34.6
	38	51.43	325.34	0.16	0.06806	0.00155	1.29014	0.03353	0.13748	0.00330	870.3	46.6	841.4	14.9	830.4	18.7

Table A1. *Cont.*

Sample	Spot	Th (ppm)	U (ppm)	Th/U	Isotope						Age (Ma)					
					^{207}Pb/^{206}Pb	1σ	^{207}Pb/^{235}U	1σ	^{206}Pb/^{238}U	1σ	^{207}Pb/^{206}Pb	1σ	^{207}Pb/^{235}U	1σ	^{206}Pb/^{238}U	1σ
Sp-a	39	603.63	1311.16	0.46	0.05143	0.00124	0.24550	0.00666	0.03462	0.00083	260.0	54.5	222.9	5.4	219.4	5.2
	41	126.70	232.29	0.55	0.15006	0.00314	8.63560	0.21170	0.41737	0.01007	2346.6	35.4	2300.3	22.3	2248.5	45.8
	43	155.26	1048.64	0.15	0.11316	0.00228	4.94386	0.11805	0.31687	0.00759	1850.7	36.0	1809.8	20.2	1774.4	37.2
	44	170.11	355.76	0.48	0.11514	0.00236	5.21752	0.12627	0.32865	0.00790	1882.0	36.5	1855.5	20.6	1831.9	38.3
	45	134.58	300.67	0.45	0.06072	0.00185	0.54767	0.01789	0.06542	0.00161	629.3	64.3	443.5	11.7	408.5	9.8
	46	793.23	890.47	0.89	0.05241	0.00132	0.26765	0.00753	0.03704	0.00090	303.5	56.3	240.8	6.0	234.4	5.6
	52	120.01	172.95	0.69	0.05624	0.00214	0.33008	0.01308	0.04257	0.00107	461.1	82.9	289.6	10.0	268.7	6.6
	53	142.72	204.66	0.70	0.10680	0.00228	4.29421	0.10734	0.29165	0.00709	1745.5	38.5	1692.3	20.6	1649.8	35.4
	56	59.90	731.29	0.08	0.08682	0.00182	2.73121	0.06763	0.22819	0.00554	1356.5	39.9	1337.0	18.4	1325.0	29.1
	59	53.56	235.97	0.23	0.07610	0.00174	1.77189	0.04669	0.16891	0.00413	1097.6	45.2	1035.2	17.1	1006.1	22.8
	61	332.25	590.25	0.56	0.05647	0.00137	0.54088	0.01490	0.06949	0.00170	470.0	53.4	439.0	9.8	433.1	10.3
	62	105.14	1170.37	0.09	0.06891	0.00145	1.25754	0.03123	0.13239	0.00323	896.0	42.7	826.8	14.1	801.5	18.4
	63	221.04	690.20	0.32	0.06405	0.00146	0.85044	0.02243	0.09633	0.00236	743.2	47.6	624.9	12.3	592.9	13.9
	68	166.91	301.47	0.55	0.11139	0.00129	4.55493	0.06387	0.29599	0.00389	1822.1	20.9	1741.1	11.7	1671.4	19.4
	69	208.79	745.91	0.28	0.07821	0.00114	1.94242	0.03196	0.17975	0.00240	1152.3	28.7	1095.8	11.0	1065.6	13.1
	72	352.93	470.22	0.75	0.08562	0.00102	2.43262	0.03470	0.20563	0.00270	1329.5	22.9	1252.3	10.3	1205.5	14.4
	73	328.09	2115.46	0.16	0.05508	0.00109	0.33877	0.00714	0.04452	0.00060	415.3	43.5	296.2	5.4	280.8	3.7
	74	75.01	173.51	0.43	0.07702	0.00151	1.82357	0.03803	0.17135	0.00239	1121.7	38.7	1054.0	13.7	1019.6	13.2
	75	185.18	406.77	0.46	0.07458	0.00099	1.67879	0.02587	0.16290	0.00215	1057.0	26.9	1000.5	9.8	972.9	11.9
	76	49.54	358.10	0.14	0.11379	0.00148	4.79205	0.07252	0.30478	0.00408	1860.8	23.3	1783.5	12.7	1715.0	20.2
	78	506.75	629.94	0.80	0.05602	0.00126	0.37892	0.00889	0.04895	0.00068	452.6	49.0	326.2	6.6	308.1	4.2
	80	281.93	1042.62	0.27	0.05164	0.00094	0.23761	0.00466	0.03329	0.00045	269.7	41.2	216.5	3.8	211.1	2.8
	81	307.15	541.57	0.57	0.06255	0.00091	0.81683	0.01339	0.09449	0.00125	693.1	30.6	606.3	7.5	582.1	7.4
	82	123.66	432.57	0.29	0.07324	0.00113	1.46956	0.02532	0.14520	0.00195	1020.5	31.0	917.9	10.4	874.0	11.0

Table A2. In situ zircon trace, rare earth elements results from the Sabah ophiolites.

Sample	Spot	Ti	Y	Zr	Nb	La	Ce	Pr	Nd	Sm	Eu	Gd	Tb	Dy	Ho	Er	Tm	Yb	Lu	Hf	Ta	Th	U
KDS-KET-a	1	19.81	1438	394683	7.68	15.46	47.65	6.05	32.77	12.95	1.63	39.75	13.45	146.10	49.81	209.73	40.49	364.25	67.57	9590	1.75	341.58	477.33
	2	7.53	901	343068	3.33	0.09	17.36	0.13	1.53	3.38	1.20	16.55	6.62	78.88	29.75	128.18	26.49	246.89	48.98	9376	0.99	195.49	409.51
	3	16.70	647	392878	3.73	5.81	21.69	1.91	11.37	3.60	0.18	11.90	4.26	55.49	21.86	103.17	21.85	214.43	41.54	10508	1.31	67.70	178.31
	4	16.51	2015	375931	2.88	5.79	19.98	2.46	16.32	10.96	0.59	49.81	16.92	196.88	73.70	307.92	58.81	505.62	92.81	7675	0.78	135.62	220.29
	5	8.71	1446	354604	2.78	1.09	12.42	0.29	2.94	6.55	0.52	32.65	10.97	131.34	51.21	216.06	43.48	425.73	75.97	8909	1.15	419.25	655.62
	6	23.61	1095	400240	1.65	0.47	11.52	0.58	3.43	4.51	1.06	20.64	7.48	99.01	37.48	164.69	35.28	340.62	65.40	11083	0.56	128.78	111.17
	7	12.05	1190	386614	1.60	0.26	11.30	0.30	3.65	4.77	1.31	26.49	9.06	110.71	41.41	177.71	36.94	342.80	66.40	10119	0.56	136.32	109.42
	8	6.68	1393	384744	9.96	3.47	14.77	1.92	13.35	8.69	1.25	32.27	11.18	125.80	46.93	202.11	41.19	385.29	72.68	11068	4.29	207.18	877.92
	9	1.54	898	378105	5.71	0.05	3.06	0.06	0.46	2.13	0.17	13.61	5.87	77.42	29.59	134.89	28.98	263.84	50.00	11349	2.83	116.81	640.33
	10	4.17	1093	355362	9.43	0.03	4.19	0.06	0.53	1.83	0.37	15.79	6.58	90.29	35.66	162.30	34.43	326.52	62.91	10665	6.11	224.08	1231.94
	11	1.90	1202	371418	10.43	2.16	11.08	1.16	6.35	3.31	0.35	16.67	7.54	99.25	39.85	175.51	38.29	352.42	66.24	11133	6.79	275.25	1362.67
	12	14.74	1192	375299	1.24	0.34	17.84	0.78	8.90	11.37	0.98	37.29	11.77	120.92	41.00	162.09	30.82	264.19	47.64	8829	0.50	186.41	185.50
	13	15.70	1637	379804	1.29	0.34	21.24	1.20	14.30	14.85	1.71	54.76	16.64	172.39	56.51	220.76	40.96	347.28	62.31	8806	0.62	279.10	263.98

Table A2. *Cont.*

Sample	Spot	Ti	Y	Zr	Nb	La	Ce	Pr	Nd	Sm	Eu	Gd	Tb	Dy	Ho	Er	Tm	Yb	Lu	Hf	Ta	Th	U
ND-KET-b	1	3.61	154	426512	0.20	0.00	5.83	0.02	0.23	0.52	0.22	2.42	0.81	9.86	4.61	25.17	6.44	80.48	20.35	10481	0.10	44.28	102.21
	2	4.21	132	420525	0.13	0.01	5.07	0.01	0.35	0.49	0.32	2.55	0.82	9.29	4.00	21.08	5.77	67.53	17.90	9173	0.08	32.66	61.31
	3	5.01	324	427812	0.11	0.00	7.10	0.06	1.53	1.88	0.92	7.36	2.23	26.75	10.08	49.18	12.34	138.63	33.55	9598	0.06	60.07	74.83
	4	7.24	503	415816	0.19	0.02	8.26	0.07	1.41	3.02	0.87	11.62	3.51	43.69	16.95	79.35	17.24	171.93	36.65	8650	0.10	37.72	43.63
	5	4.04	238	432252	0.14	0.01	5.00	0.04	0.73	1.10	0.44	4.40	1.46	16.91	7.12	37.11	9.58	118.97	30.65	10092	0.07	43.95	77.43
	6	4.56	209	427092	0.19	0.00	5.37	0.04	0.53	0.78	0.41	3.92	1.27	15.68	6.39	31.79	8.36	102.04	24.51	9495	0.11	31.28	52.30
	7	8.27	746	433290	0.23	0.01	9.64	0.09	2.40	4.15	1.56	19.28	5.91	69.52	24.75	114.15	24.20	235.61	46.87	8878	0.10	33.61	40.05
	8	4.32	150	418054	0.23	0.01	6.37	0.01	0.18	0.46	0.25	2.09	0.77	9.97	4.49	23.75	5.95	70.62	16.91	9739	0.10	26.72	56.62
	9	5.12	121	437354	0.11	0.02	4.68	0.01	0.18	0.43	0.20	1.60	0.65	8.93	3.84	18.53	4.86	58.43	13.79	9671	0.06	19.62	43.69
	10	3.45	107	424361	0.18	0.00	4.76	0.02	0.10	0.23	0.14	1.33	0.57	7.25	3.13	16.74	4.76	58.54	14.90	10225	0.10	35.16	79.97
	11	11.72	1043	423879	0.16	0.01	11.22	0.21	3.04	5.61	1.96	25.25	8.13	94.75	35.15	152.67	31.38	308.49	59.81	8263	0.12	50.16	49.83
	12	8.10	566	432022	0.15	0.00	8.25	0.05	1.15	2.90	0.97	12.21	4.14	48.56	18.59	85.67	18.60	192.23	38.64	9225	0.08	28.95	37.75
	13	5.86	314	420035	0.34	0.03	8.48	0.04	0.49	1.25	0.43	5.73	2.13	24.19	9.58	49.69	11.17	124.14	26.90	9238	0.12	30.20	48.07
	14	6.28	296	422263	0.27	0.00	8.71	0.02	0.19	1.00	0.28	4.75	1.89	21.80	9.56	46.08	10.68	112.65	24.21	9450	0.09	26.51	44.22
	15	4.07	207	420713	0.17	0.02	4.86	0.05	0.72	0.97	0.50	4.27	1.28	14.63	6.57	33.61	8.64	106.88	26.88	10020	0.08	38.86	71.64
	16	4.98	141	421475	0.12	0.00	4.50	0.00	0.24	0.39	0.23	2.39	0.85	10.43	4.42	23.75	6.08	77.24	19.45	9940	0.10	33.59	65.06
	18	4.06	144	431456	0.20	0.01	5.37	0.02	0.20	0.45	0.29	1.84	0.79	10.31	4.38	22.31	6.02	78.12	19.25	10913	0.15	42.24	96.02
	19	9.33	413	427692	0.29	0.00	7.86	0.02	0.55	1.84	0.54	9.61	3.09	36.02	13.79	63.95	13.76	143.85	28.55	8619	0.09	18.62	27.09
	20	3.94	170	412999	0.17	0.00	4.46	0.02	0.39	0.52	0.34	2.26	0.92	11.91	5.22	27.76	7.40	89.97	24.18	10006	0.10	34.97	71.06
	21	10.12	435	412936	0.24	0.00	7.51	0.08	0.88	2.44	0.81	9.09	3.13	34.95	13.26	64.54	15.64	167.25	37.13	9257	0.09	32.62	46.99
	22	4.16	216	445649	0.21	0.00	6.42	0.01	0.39	0.36	0.22	2.95	1.13	14.69	6.15	34.85	9.44	120.94	31.15	11788	0.13	51.73	117.70
	23	9.84	1010	418010	0.13	0.01	10.58	0.15	3.21	4.72	1.68	21.35	7.21	85.16	34.20	156.96	32.95	322.58	65.02	8243	0.12	53.41	60.88
	24	7.87	415	421963	0.25	0.00	7.20	0.02	0.46	1.37	0.61	8.54	2.74	34.62	14.04	63.59	14.18	145.29	29.66	8416	0.07	16.51	25.65
	25	7.00	374	436179	0.21	0.02	5.93	0.05	0.57	1.44	0.46	7.03	2.38	29.16	11.86	57.91	13.61	146.69	31.28	9857	0.09	16.83	32.55
Sp-a	3	3.12	591	438782	0.79	0.00	4.01	0.05	0.86	1.93	0.78	10.18	4.13	50.29	19.30	87.91	18.55	184.49	37.77	8272	0.31	36.78	106.41
	4	10.07	3059	452050	4.25	4.30	54.31	1.80	11.43	11.06	1.81	58.95	20.66	248.06	94.77	425.97	88.13	839.73	158.17	9886	1.18	905.03	820.29
	5	50.62	1019	466409	1.54	0.14	15.43	0.48	7.41	11.10	1.77	40.43	11.86	114.00	36.06	134.37	24.26	207.21	35.51	8555	0.52	149.06	179.19
	6	6.75	394	460673	1.58	39.50	83.35	6.44	24.64	4.87	1.16	8.71	2.63	29.80	11.90	59.76	14.14	164.16	36.96	8746	0.61	367.88	358.74
	7	3.10	618	432450	1.88	0.57	13.13	0.18	1.24	1.89	0.50	9.73	3.89	47.68	18.86	92.98	21.16	225.49	47.23	10271	1.06	346.16	880.45
	9	5.10	1112	446530	3.53	0.03	6.83	0.03	0.78	2.83	0.41	18.83	7.64	96.38	38.37	173.47	35.03	330.82	60.41	9970	1.56	102.74	208.65
	10	16.37	821	460972	2.08	0.01	12.07	0.06	1.04	2.79	0.26	15.53	6.01	73.19	28.22	126.73	26.35	248.86	46.85	10260	0.88	89.98	95.24
	11	5.50	363	467612	0.97	0.02	14.65	0.16	2.62	3.69	0.85	12.55	3.66	35.73	11.80	47.95	9.64	90.55	16.44	9823	0.28	117.03	195.55
	12	3.49	1469	473310	3.36	0.19	26.29	0.15	1.74	4.20	1.13	21.16	8.61	114.10	46.36	226.22	51.73	544.37	112.95	9545	0.80	469.53	616.46
	14	4.23	607	453292	0.83	0.01	4.13	0.03	0.74	1.94	0.22	10.89	4.47	51.04	18.69	89.86	21.31	231.00	46.85	11842	0.73	59.41	505.74
	16	9.48	612	434535	3.79	0.02	20.26	0.08	1.26	2.46	0.49	13.43	4.75	53.83	20.13	90.44	19.33	190.22	36.50	9501	1.74	261.27	708.97
	17	12.86	388	444766	3.20	0.01	7.85	0.04	0.89	1.28	0.45	7.18	2.66	33.36	12.89	60.53	13.36	138.26	28.05	9014	1.26	120.55	347.80
	19	6.18	721	450530	2.15	0.83	14.29	0.32	2.73	2.93	0.36	14.47	5.20	62.55	24.45	109.65	23.02	215.95	42.34	8945	0.86	175.29	329.91
	20	23.87	1806	426531	0.92	0.32	19.67	0.23	3.26	6.22	1.73	33.38	11.80	142.10	55.78	259.71	55.31	553.53	109.65	8990	0.33	257.34	286.23
	21	9.91	616	450675	0.78	4.28	22.18	1.33	6.86	3.80	0.69	13.85	4.72	52.96	19.82	89.81	18.74	181.15	35.32	9329	0.34	101.71	198.76
	22	4.91	1229	467309	1.04	6.48	28.39	1.78	8.74	5.00	1.33	20.31	7.13	90.45	38.06	193.12	46.19	514.90	116.07	9691	0.38	295.25	404.24
	27	4.30	981	438229	4.32	0.00	7.72	0.05	0.98	2.75	0.06	17.74	7.12	86.85	33.94	152.89	31.37	288.98	52.63	10766	1.89	193.75	960.37
	28	5.46	962	453925	2.68	0.27	19.04	0.15	1.66	2.60	0.92	14.45	5.43	71.08	30.29	152.75	36.31	392.24	86.31	9463	0.79	150.79	226.46
	30	18.42	1559	450910	0.73	0.03	1.82	0.17	3.30	6.99	0.53	38.79	13.88	156.03	54.03	216.17	41.98	375.97	66.23	10140	0.34	56.80	273.42
	31	16.93	933	442393	0.59	0.03	11.22	0.12	2.28	4.05	0.91	20.10	6.98	81.72	31.26	137.10	28.81	278.82	54.03	8493	0.25	82.04	74.70
	32	3.91	1033	440481	2.29	0.01	4.57	0.07	1.32	3.08	0.37	19.14	7.06	89.46	35.86	162.23	33.92	319.70	62.10	8077	0.67	118.11	324.42
	33	17.84	805	443119	2.27	7.58	26.69	3.09	15.05	8.52	0.61	26.26	7.77	80.77	27.84	114.87	23.05	215.27	39.86	9646	0.89	181.62	366.07
	34	4.89	399	445732	2.09	0.00	12.73	0.02	0.45	1.50	0.26	7.99	3.02	35.74	13.21	59.57	12.33	121.47	23.52	10718	1.29	84.32	229.97
	38	6.28	851	437276	0.73	0.00	1.02	0.05	0.96	3.14	0.09	19.32	7.97	88.40	27.96	104.79	19.24	164.24	27.95	11189	0.44	51.43	325.34

Table A2. *Cont.*

Sample	Spot	Ti	Y	Zr	Nb	La	Ce	Pr	Nd	Sm	Eu	Gd	Tb	Dy	Ho	Er	Tm	Yb	Lu	Hf	Ta	Th	U
Sp-a	39	7.32	745	445854	2.10	17.47	61.12	4.20	17.57	5.68	0.93	17.11	5.63	64.10	23.93	109.20	23.86	235.88	46.84	10559	1.32	603.63	1311.16
	41	5.76	653	458413	1.09	0.05	11.18	0.17	2.53	3.27	1.47	16.55	5.68	63.66	21.17	93.30	19.64	193.10	35.94	10032	0.45	126.70	232.29
	43	6.26	1088	454686	1.56	0.08	3.31	0.18	2.11	4.05	1.54	21.39	8.73	101.98	36.22	156.88	32.43	310.12	59.10	11344	1.30	155.26	1048.64
	44	7.46	690	458818	1.94	4.22	36.69	1.28	7.17	3.99	1.36	15.35	5.06	57.88	21.58	98.88	21.55	218.59	43.54	9258	0.92	170.11	355.76
	45	15.46	2112	451888	1.76	0.05	5.79	0.31	3.55	6.48	1.72	35.17	15.00	181.08	68.20	301.87	62.08	584.36	106.75	10115	1.04	134.58	300.67
	46	18.99	2044	447242	5.09	8.30	61.48	3.89	23.90	16.53	5.38	55.28	19.68	200.47	63.97	251.95	49.57	457.16	82.44	9906	1.67	793.23	890.47
	52	12.25	1015	444900	1.09	0.19	19.28	0.25	3.34	5.29	0.82	22.95	8.08	89.19	33.46	148.89	30.88	301.32	58.76	8223	0.42	120.01	172.95
	53	22.75	1277	449625	1.46	0.05	5.50	0.25	3.60	6.69	1.09	34.17	11.27	124.84	45.12	189.76	37.10	343.36	63.84	9572	0.68	142.72	204.66
	56	4.83	947	463033	1.72	0.01	11.97	0.03	0.62	1.40	0.43	9.91	5.19	71.51	29.86	143.82	33.54	360.81	69.16	12181	1.29	59.90	731.29
	59	7.96	699	448051	0.67	0.07	2.46	0.07	0.91	2.35	0.41	12.46	5.03	63.44	23.56	108.09	23.09	228.06	43.20	9072	0.29	53.56	235.97
	61	7.08	1189	449210	2.00	0.05	16.65	0.30	3.92	6.74	2.00	27.38	9.33	106.41	38.41	175.58	37.86	386.83	77.09	10000	1.05	332.25	590.25
	62	6.66	1032	460399	21.97	0.04	2.46	0.17	2.13	3.87	1.52	18.38	6.93	79.22	31.97	164.99	44.54	547.79	129.60	12915	39.10	105.14	1170.37
	63	11.78	821	475169	2.49	0.02	6.48	0.07	1.22	2.65	0.44	13.95	5.52	67.80	25.65	117.25	25.45	249.27	47.52	11543	1.33	221.04	690.20
	68	24.09	1589	459340	1.62	0.27	9.97	0.76	10.61	16.63	3.31	63.91	19.25	185.81	55.60	202.78	36.83	320.18	53.63	10011	0.80	166.91	301.47
	69	15.20	1504	467637	2.18	0.42	8.58	1.01	9.30	12.52	5.35	50.11	17.45	174.14	50.72	177.90	31.20	260.88	44.41	11576	1.32	208.79	745.91
	72	13.77	2357	455776	5.37	0.12	13.31	0.36	5.35	9.61	0.72	50.35	18.24	211.05	78.15	327.80	63.47	574.15	102.73	9269	2.22	352.93	470.22
	73	11.03	2086	504728	8.25	0.30	12.14	0.15	1.58	4.75	0.99	38.61	16.82	200.51	70.12	298.14	62.74	586.93	103.37	16414	4.64	328.09	2115.45
	74	14.23	1526	477697	1.17	0.09	2.49	0.13	2.00	4.64	0.41	30.44	11.50	144.08	52.55	224.81	43.70	400.68	69.17	11498	0.60	75.01	173.51
	75	11.35	598	471667	2.30	3.60	19.78	1.13	5.80	3.43	0.39	13.15	4.59	53.84	20.01	89.63	18.74	178.84	32.76	10639	1.02	185.18	406.77
	76	14.63	1518	472718	0.67	0.29	1.19	0.13	1.53	3.44	0.23	25.06	11.06	135.39	49.98	216.25	44.41	409.86	75.39	12207	0.36	49.54	358.10
	78	5.98	1397	475165	5.93	0.31	63.56	0.40	4.80	8.32	3.20	36.34	12.68	134.12	45.95	193.05	39.62	384.79	71.51	11021	1.24	506.75	629.94
	80	10.63	1566	467015	3.14	0.22	4.79	0.18	2.67	5.35	0.18	29.31	11.54	142.68	54.03	239.92	50.63	476.70	85.56	11870	2.55	281.93	1042.62
	81	32.03	1508	470778	9.50	0.92	38.81	2.36	22.03	23.66	9.35	57.26	18.07	173.42	48.86	182.65	34.42	312.31	52.59	9568	3.72	307.15	541.57
	82	10.38	638	486158	1.47	0.08	12.47	0.08	0.83	2.80	0.76	17.09	6.13	63.84	20.89	85.27	17.66	174.59	31.56	11977	0.82	123.66	432.57

Table A3. Whole-rock major, trace, rare earth elements results for mafic-ultramafic rocks from the Sabah ophiolites.

Sample		SiO_2	Al_2O_3	Fe_2O_3	FeO	CaO	MgO	K_2O	Na_2O	TiO_2	P_2O_5	MnO	LOI	Total	Li	Be	Sc	V	Cr
KM-KET-1	basalt	54.71	16.36	2.53	2.36	9.67	4.48	0.38	3.55	0.87	0.07	0.10	4.79	99.87	24.43	0.59	17.17	184.20	215.10
KM-KET-2		50.31	16.83	3.48	2.28	11.70	5.33	0.16	2.97	0.92	0.08	0.11	5.46	99.89	23.23	0.69	26.63	161.81	226.24
KM-KET-3		50.39	16.82	3.67	2.11	11.68	5.30	0.16	2.96	0.92	0.08	0.11	5.45	99.89	22.84	0.65	28.21	154.64	202.46
KM-KET-4		49.84	14.61	3.19	4.89	8.37	7.75	0.42	4.55	1.32	0.12	0.17	4.06	99.85	38.80	0.38	38.06	227.75	315.75
KDS-KET-1	serpentinized peridotite	41.42	0.68	6.64	1.36	0.03	36.64	0.00	0.06	0.00	0.01	0.10	13.09	100.02	0.69	0.00	9.16	1.99	2182.00
KDS-KET-2		41.30	1.02	5.45	2.24	0.07	36.55	0.00	0.00	0.00	0.00	0.08	12.51	99.47	5.28	0.18	11.56	68.12	2937.05
KDS-KET-3		40.73	0.72	5.79	1.77	0.07	37.19	0.00	0.00	0.00	0.00	0.08	13.01	99.55	1.91	0.03	10.20	47.01	1997.71
BLR-CS-1	basalt	57.54	13.58	2.73	4.17	8.23	5.42	0.01	3.66	0.89	0.07	0.14	3.39	99.83	3.67	0.35	3.38	274.50	215.10
BLR-CS-2		51.06	14.40	3.48	5.48	10.00	7.10	0.15	3.60	1.33	0.11	0.20	2.81	99.71	18.82	0.50	5.11	297.60	300.60
BLR-CS-3		51.45	14.89	3.20	5.00	9.47	6.26	0.02	4.56	1.32	0.08	0.17	3.47	99.88	11.95	0.44	4.83	314.40	146.30
BLR-CS-4		51.57	14.74	4.55	4.68	8.86	6.01	0.76	4.43	1.25	0.11	0.41	1.98	99.87	11.53	0.45	38.28	259.17	238.26
BLR-KET-1	serpentinized peridotite	45.29	0.89	6.68	1.27	0.08	32.05	0.00	0.06	0.00	0.01	0.09	13.59	100.03	1.33	0.02	3.50	16.83	2645.00
BLR-KET-2		43.50	1.00	5.99	1.85	0.18	33.93	0.00	0.00	0.00	0.00	0.09	12.77	99.51	10.69	0.10	10.40	54.65	2444.59
BLR-KET-3		47.34	0.68	6.23	1.23	0.12	31.27	0.01	0.03	0.00	0.00	0.08	12.33	99.44	4.14	0.05	8.40	64.34	3209.56

Table A3. *Cont.*

Sample		Co	Ni	Cu	Zn	Ga	Rb	Sr	Y	Zr	Nb	Mo	Cd	Cs	Ba	La	Ce	Pr	Nd
KM-KET-1	basalt	23.53	89.33	51.06	50.59	16.25	7.70	119.00	14.44	91.70	4.40	0.51	0.76	0.13	16.07	4.52	10.58	1.51	6.94
KM-KET-2		30.47	117.20	39.16	59.16	18.41	12.60	85.83	16.30	95.74	4.72	0.37	0.13	0.37	17.85	5.96	13.34	1.54	7.30
KM-KET-3		29.37	102.25	34.41	50.03	17.34	7.84	80.51	15.32	96.93	4.58	0.39	0.12	0.39	18.75	5.69	12.91	1.51	7.22
KM-KET-4		40.80	118.56	60.41	65.54	11.20	6.15	169.83	29.53	92.89	1.82	0.71	0.10	0.98	40.80	3.42	10.71	1.55	8.85
KDS-KET-1	serpentinized peridotite	74.24	1749.00	7.13	46.22	0.93	0.37	2.78	0.22	0.43	0.05	0.25	0.02	0.02	2.67	0.15	1.10	0.04	0.13
KDS-KET-2		69.34	1072.86	13.61	38.10	1.62	10.24	7.11	1.87	49.41	0.90	0.77	0.19	0.85	14.40	1.72	3.15	0.33	1.24
KDS-KET-3		72.20	1297.77	9.74	38.78	1.05	3.83	4.32	0.99	45.79	0.30	0.28	0.02	0.43	6.19	0.82	1.50	0.17	0.65
BLR-CS-1	basalt	29.56	80.86	50.00	63.35	16.05	1.31	66.12	13.36	65.56	1.04	0.64	0.56	0.03	5.88	1.61	5.51	0.98	5.32
BLR-CS-2		38.65	80.19	48.89	74.57	18.67	5.16	124.60	21.00	96.40	1.72	0.49	0.99	0.14	10.18	2.76	9.32	1.61	8.69
BLR-CS-3		34.82	53.90	60.44	75.95	18.56	1.41	114.30	19.65	91.75	1.45	0.54	0.91	0.04	11.42	1.99	6.95	1.25	6.85
BLR-CS-4		42.71	61.15	56.39	205.79	15.90	18.32	143.14	29.14	93.83	1.60	0.37	0.09	0.68	25.30	3.73	11.44	1.54	8.61
BLR-KET-1	serpentinized peridotite	64.79	1680.00	13.77	53.06	0.98	0.42	1.25	0.26	0.64	0.07	0.13	0.02	0.04	1.56	0.12	0.29	0.04	0.12
BLR-KET-2		65.41	1216.93	13.46	44.09	1.73	1.66	6.10	0.75	2.44	0.33	0.13	0.02	0.06	23.26	0.68	1.49	0.16	0.60
BLR-KET-3		83.88	1431.07	7.30	153.51	1.21	1.58	6.50	0.66	42.45	0.36	0.15	0.02	0.48	13.26	0.93	1.77	0.20	0.77

Sample		Sm	Eu	Gd	Tb	Dy	Ho	Er	Tm	Yb	Lu	Hf	Ta	W	Tl	Pb	Bi	Th	U
KM-KET-1	basalt	2.12	0.87	2.67	0.50	3.15	0.70	2.00	0.32	1.91	0.32	3.51	1.42	0.28	0.17	1.50	0.05	0.52	0.17
KM-KET-2		1.87	0.70	2.03	0.45	2.77	0.54	1.57	0.26	1.70	0.25	3.02	0.73	0.63	0.06	3.14	0.01	0.74	0.18
KM-KET-3		1.83	0.69	2.02	0.44	2.70	0.53	1.52	0.26	1.68	0.24	2.97	2.86	0.48	0.05	3.20	0.01	0.64	0.19
KM-KET-4		2.85	1.02	3.24	0.77	4.86	0.94	2.75	0.45	2.96	0.41	3.09	1.02	0.50	0.07	2.41	0.02	0.22	0.12
KDS-KET-1	serpentinized peridotite	0.03	0.01	0.04	0.01	0.04	0.01	0.03	0.01	0.05	0.01	0.02	0.03	0.05	0.09	0.25	0.00	0.22	0.05
KDS-KET-2		0.22	0.03	0.20	0.04	0.22	0.04	0.14	0.04	0.18	0.03	1.18	0.29	0.52	0.09	2.18	0.02	1.49	0.26
KDS-KET-3		0.11	0.02	0.10	0.02	0.12	0.02	0.08	0.04	0.12	0.02	1.11	1.00	0.76	0.05	4.89	0.03	0.51	0.10
BLR-CS-1	basalt	1.92	0.76	2.74	0.53	3.61	0.84	2.50	0.40	2.43	0.39	2.75	0.86	0.22	0.15	0.79	0.03	0.08	0.46
BLR-CS-2		3.06	1.16	4.08	0.78	5.25	1.16	3.36	0.51	3.16	0.48	3.64	0.61	0.22	0.13	0.84	0.02	0.12	0.13
BLR-CS-3		2.61	1.09	3.66	0.72	4.63	1.07	3.12	0.48	3.00	0.47	3.63	0.27	0.15	0.15	0.76	0.02	0.07	0.14
BLR-CS-4		2.76	1.00	3.21	0.75	4.82	0.97	2.80	0.45	3.03	0.44	3.07	1.06	0.87	0.08	2.39	0.01	0.29	0.17
BLR-KET-1	serpentinized peridotite	0.05	0.02	0.04	0.02	0.06	0.03	0.05	0.02	0.07	0.02	0.03	0.13	0.09	0.12	0.25	0.02	0.08	0.03
BLR-KET-2		0.11	0.03	0.11	0.02	0.12	0.02	0.07	0.03	0.09	0.01	0.08	0.69	0.74	0.05	2.93	0.19	0.16	0.04
BLR-KET-3		0.12	0.03	0.11	0.02	0.10	0.02	0.07	0.03	0.09	0.02	1.01	0.89	1.11	0.04	2.82	0.01	0.31	0.09

Sample		SiO_2	Al_2O_3	Fe_2O_3	FeO	CaO	MgO	K_2O	Na_2O	TiO_2	P_2O_5	MnO	LOI	Total	Li	Be	Sc	V	Cr
BLR-KET-4	gabbro	50.53	14.55	2.85	5.98	7.78	8.38	0.70	3.87	1.14	0.04	0.19	3.90	99.92	6.72	0.26	37.24	292.20	158.50
BLR-KET-5		48.93	14.85	3.08	6.13	8.81	8.66	0.65	3.46	1.02	0.08	0.27	3.28	99.89	9.46	0.35	36.23	252.27	202.92
BLR-KET-6		53.86	14.72	2.71	4.71	8.33	5.93	0.14	5.49	1.39	0.10	0.14	2.31	99.85	3.09	0.48	1.62	269.60	228.10
BLR-KET-7		50.02	15.72	2.06	5.62	9.77	9.10	0.04	3.63	0.86	0.07	0.17	2.17	99.86	8.07	0.30	32.96	199.54	401.10
BLR-KET-8		52.33	15.40	3.49	6.62	3.70	6.23	0.38	6.11	1.39	0.05	0.41	3.04	99.89	45.62	0.53	31.92	279.61	50.59
ND-KET-1	serpentinized peridotite	45.84	0.41	8.92	0.82	0.02	31.33	0.00	0.06	0.01	0.01	0.12	12.05	99.59	0.20	0.02	3.51	5.08	1871.00
ND-KET-2		45.74	0.35	9.42	0.32	0.06	30.39	0.00	0.06	0.01	0.01	0.12	13.22	99.69	0.15	0.01	2.05	1.54	1387.00
ND-KET-3		42.27	1.65	3.21	3.85	1.37	36.86	0.00	0.12	0.01	0.01	0.11	10.24	99.70	0.09	0.05	3.57	32.20	2488.00
ND-KET-4		40.88	1.81	3.27	3.58	2.11	37.40	0.00	0.05	0.02	0.00	0.11	9.84	99.48	3.73	0.08	14.92	60.21	2710.83
ND-KET-5	basalt	58.94	16.48	1.90	3.71	3.59	4.94	0.96	5.06	0.75	0.03	0.13	3.34	99.84	5.61	1.15	6.38	147.40	132.50
ND-KET-6		50.64	16.88	2.75	5.42	7.50	6.93	0.28	4.65	0.74	0.10	0.18	3.68	99.74	4.76	0.49	5.74	298.30	85.83
ND-KET-7		59.83	15.96	3.05	3.85	6.47	3.12	2.19	2.50	0.67	0.09	0.18	1.83	99.76	8.36	0.95	9.89	236.40	24.65
ND-KET-8		55.00	16.80	3.72	5.25	3.49	5.07	1.29	2.87	1.10	0.11	0.18	4.93	99.82	10.20	0.60	12.62	354.10	17.17

Table A3. *Cont.*

Sample		Co	Ni	Cu	Zn	Ga	Rb	Sr	Y	Zr	Nb	Mo	Cd	Cs	Ba	La	Ce	Pr	Nd
BLR-KET-4	gabbro	38.73	64.15	74.68	82.15	15.19	4.59	118.90	18.78	55.09	0.75	0.62	0.59	0.05	14.68	1.32	4.47	0.79	4.49
BLR-KET-5		44.78	75.25	73.70	103.73	15.44	10.79	108.76	24.85	74.51	1.10	0.36	0.06	0.45	20.46	2.79	8.33	1.15	6.47
BLR-KET-6		30.14	61.87	49.87	61.59	13.97	6.07	159.50	14.83	97.45	2.12	0.41	0.87	0.31	20.27	2.63	9.25	1.47	7.86
BLR-KET-7		42.72	155.78	8.53	54.46	14.41	1.95	134.93	22.29	80.16	1.01	0.30	0.08	0.57	16.18	2.83	7.88	1.12	6.28
BLR-KET-8		31.19	34.25	36.05	131.87	14.87	9.15	91.68	26.55	85.99	1.55	0.57	0.05	2.72	51.07	3.05	9.37	1.59	8.22
ND-KET-1	serpentinized peridotite	106.50	2271.00	4.22	80.32	0.78	0.34	1.53	0.39	0.71	0.19	0.12	0.00	0.03	2.86	0.40	0.12	0.07	0.26
ND-KET-2		102.50	2094.00	3.60	55.58	0.64	0.64	3.45	0.26	0.37	0.14	0.15	0.00	0.02	2.84	0.22	0.51	0.05	0.16
ND-KET-3		98.02	1812.00	4.51	50.51	1.53	0.81	4.05	0.61	0.92	0.30	0.28	0.03	0.04	1.91	0.20	0.49	0.07	0.23
ND-KET-4		76.94	1282.56	3.17	78.71	2.36	1.38	11.06	1.86	49.92	0.51	0.14	0.02	0.61	6.40	1.19	2.46	0.28	1.12
ND-KET-5	basalt	18.73	88.14	18.03	67.40	14.15	16.57	310.80	16.43	124.00	2.58	0.40	0.94	0.33	118.40	8.35	21.98	2.89	12.59
ND-KET-6		37.38	56.35	91.98	127.90	14.26	5.00	705.50	10.66	61.39	1.37	0.35	0.72	0.38	107.20	7.09	17.86	2.47	11.16
ND-KET-7		20.46	11.93	47.69	76.85	17.55	33.12	224.30	18.35	116.10	3.42	1.76	1.09	7.55	202.30	10.92	27.22	3.29	13.62
ND-KET-8		21.48	12.51	10.63	116.40	15.97	29.46	235.80	24.38	102.30	2.19	0.33	0.95	0.51	102.00	11.55	28.90	3.86	18.12

Sample		Sm	Eu	Gd	Tb	Dy	Ho	Er	Tm	Yb	Lu	Hf	Ta	W	Tl	Pb	Bi	Th	U
BLR-KET-4	gabbro	1.77	0.89	2.75	0.56	3.79	0.84	2.46	0.36	2.34	0.34	2.30	0.10	0.08	0.11	0.86	0.01	0.09	0.05
BLR-KET-5		2.17	0.81	2.63	0.63	4.02	0.82	2.36	0.39	2.58	0.36	2.54	0.89	0.82	0.06	3.89	0.01	0.35	0.13
BLR-KET-6		2.65	1.02	3.59	0.68	4.52	0.99	2.86	0.43	2.71	0.42	3.65	0.37	0.15	0.15	0.80	0.02	0.10	0.12
BLR-KET-7		2.04	0.78	2.42	0.56	3.65	0.72	2.11	0.35	2.26	0.34	2.67	5.27	0.65	0.05	3.67	0.01	0.42	0.12
BLR-KET-8		2.30	0.93	2.67	0.66	4.43	0.87	2.59	0.44	3.04	0.44	2.99	1.35	0.76	0.10	4.46	0.01	0.31	0.12
ND-KET-1	serpentinized peridotite	0.05	0.03	0.05	0.02	0.05	0.02	0.05	0.02	0.06	0.02	0.03	0.33	0.18	0.13	0.18	0.02	0.03	0.02
ND-KET-2		0.04	0.02	0.05	0.02	0.04	0.02	0.04	0.01	0.05	0.02	0.02	0.31	0.27	0.13	0.21	0.02	0.07	0.03
ND-KET-3		0.07	0.05	0.09	0.02	0.11	0.04	0.10	0.03	0.12	0.03	0.04	0.47	0.18	0.13	0.46	0.02	0.03	0.02
ND-KET-4		0.21	0.07	0.21	0.04	0.28	0.05	0.21	0.05	0.21	0.03	1.23	0.81	0.65	0.04	6.53	0.00	0.33	0.10
ND-KET-5	basalt	3.16	1.13	3.49	0.57	3.36	0.71	2.08	0.32	1.96	0.33	4.78	0.31	0.32	0.24	4.29	0.04	2.33	0.99
ND-KET-6		2.76	1.04	2.97	0.49	2.95	0.64	1.77	0.29	1.72	0.26	2.32	0.22	0.20	0.17	3.65	0.03	0.41	0.49
ND-KET-7		3.35	1.02	3.74	0.64	4.03	0.91	2.65	0.42	2.67	0.43	4.86	0.41	1.18	0.69	9.62	0.12	6.19	1.96
ND-KET-8		4.72	1.67	5.05	0.82	5.11	1.08	3.13	0.47	2.98	0.47	3.92	0.22	0.22	0.36	3.25	0.04	1.10	1.00

Table A4. Sr-Nd-Pb isotopic results for mafic-ultramafic rocks from the Sabah ophiolites.

Sample		**Age (Ma)**	**Rb (ppm)**	**Sr (ppm)**	**^{87}Rb/^{86}Sr**	**^{87}Sr/^{86}Sr**	**Sm (ppm)**	**Nd (ppm)**	**^{147}Sm/^{144}Nd**	**^{143}Nd/^{144}Nd**	**I_{Sr}**	**$\varepsilon_{Sr}(0)$**	**$\varepsilon_{Sr}(t)$**	**I_{Nd}**	**TDM (Ma)**	**T2DM (Ma)**	**$\varepsilon_{Nd}(0)$**	**εNd(t)**
KM-KET-2	basalt	248	12.60	85.83	0.4250	0.70481	1.87	7.30	0.1550	0.51297	0.70331	4.4	−12.8	0.51271	481	391	6.40	7.72
KM-KET-3		248	7.84	80.51	0.2820	0.70481	1.83	7.22	0.1536	0.51276	0.70382	4.4	−5.5	0.51251	1004	723	2.28	3.66
BLR-KET-5	gabbro	248	10.79	134.93	0.2315	0.70470	2.04	6.28	0.1964	0.51309	0.70388	2.8	−4.7	0.51277	582	308	8.72	8.73
BLR-KET-6		248	6.07	91.68	0.1917	0.70758	2.30	8.22	0.1693	0.51279	0.70691	43.8	38.4	0.51251	1248	712	2.91	3.77
Sample		**Age (Ma)**	**U (ppm)**	**Th (ppm)**	**Pb (ppm)**	**^{206}Pb/^{204}Pb**	**^{207}Pb/^{204}Pb**	**^{208}Pb/^{204}Pb**	**^{206}Pb/^{207}Pb**	**$\triangle\alpha$**	**$\triangle\beta$**	**$\triangle\gamma$**	**(^{206}Pb/^{204}Pb)i**		**(^{207}Pb/^{204}Pb)i**		**(^{208}Pb/^{204}Pb)i**	
KM-KET-2	basalt	248	0.18	0.74	3.14	18.4295	15.5279	38.2362	1.1869	80.96	13.7	31.14	18.284		15.520		38.045	
KM-KET-3		248	0.19	0.64	3.20	18.4422	15.5272	38.2411	1.1877	81.71	13.66	31.27	18.296		15.520		38.079	
BLR-KET-5	gabbro	248	0.13	0.35	3.89	18.3713	15.6368	38.5060	1.1749	77.55	20.81	38.41	18.285		15.632		38.434	
BLR-KET-6		248	0.12	0.10	0.80	16.5876	15.4213	36.3026	1.0756	−27.07	6.74	−21.01	16.244		15.404		36.207	
Sample		**Age (Ma)**	**Sm (ppm)**	**Nd (ppm)**	**^{147}Sm/^{144}Nd**	**^{143}Nd/^{144}Nd**	**I_{Nd}**	**TDM (Ma)**	**T2DM (Ma)**	**εNd(0)**	**εNd(t)**							
BLR-KET-4	gabbro	248	2.17	6.47	0.2026	0.51304	0.51272	1453	388	7.94	7.75							
KDS-KET-2	serpentinized peridotite	248	0.22	1.24	0.1065	0.51203	0.51185	1595	1757	−11.92	−9.07							
KDS-KET-3		248	0.11	0.65	0.1037	0.51197	0.51180	1631	1838	−13.00	−10.07							
BLR-KET-2		248	0.11	0.60	0.1066	0.51161	0.51143	2192	2424	−20.15	−17.31							
BLR-KET-3		248	0.12	0.77	0.0947	0.51161	0.51146	1962	2379	−19.98	−16.76							
ND-KET-4		248	0.21	1.12	0.1131	0.51248	0.51230	1012	1051	−3.02	−0.38							

Table A5. In situ zircon Lu-Hf isotopic results for mafic rocks from the Sabah ophiolites.

Sample		**Age (Ma)**	**^{176}Hf/^{177}Hf**	**^{176}Lu/^{177}Hf**	**^{176}Yb/^{177}Hf**	**ε_{Hf} Present**	**^{176}/^{177}Hf (t) CHUR**	**^{176}Hf/^{177}Hf (t)**	**ε_{Hf} (t)**	**ε_{Hf} (t) Error**	**TDM (Ma)**	**TDMC (Ma)**	**fs**
KDS-KET-a	2	256.6	0.282331	0.001321	0.037192	−15.6	0.28	0.282324	−10.2	1.02	1312	1929	−0.96
	3	247.3	0.282433	0.001333	0.038162	−12.0	0.28	0.282427	−6.8	0.76	1168	1706	−0.96
	4	248.9	0.282940	0.001810	0.055852	6.0	0.28	0.282932	11.1	1.05	451	566	−0.95
	5	246.2	0.282427	0.001431	0.042237	−12.2	0.28	0.282420	−7.0	0.75	1180	1721	−0.96
	6	440.9	0.282369	0.001797	0.053277	−14.3	0.28	0.282354	−5.1	0.73	1275	1745	−0.95
	7	461.9	0.282361	0.001089	0.030245	−14.5	0.28	0.282351	−4.7	0.83	1262	1737	−0.97
	8	243.7	0.282374	0.000995	0.030416	−14.1	0.28	0.282370	−8.9	0.55	1240	1836	−0.97
	9	254.5	0.282388	0.000827	0.024901	−13.6	0.28	0.282384	−8.1	0.62	1215	1797	−0.98
	10	251.2	0.282449	0.001085	0.032591	−11.4	0.28	0.282444	−6.1	1.23	1138	1665	−0.97
	11	244.7	0.282364	0.001133	0.033215	−14.4	0.28	0.282358	−9.3	0.71	1259	1860	−0.97
	12	1777.3	0.281595	0.001290	0.040643	−41.6	0.28	0.281552	−3.6	1.04	2337	2665	−0.96
	13	1722.6	0.281465	0.000631	0.019943	−46.2	0.28	0.281445	−8.6	1.05	2473	2933	−0.98

References

1. Colman, R.G. The diversity of ophiolites. *Geol. Mijnb.* **1984**, *63*, 144–150.
2. Stern, R.J. Subduction initiation: Spontaneous and induced. *Earth Planet. Sci. Lett.* **2004**, *226*, 275–292. [CrossRef]
3. Pearce, J.A. Basalt geochemistry used to investigate past tectonic environments on Cyprus. *Tectonophysics* **1975**, *25*, 41–67. [CrossRef]
4. Moores, E.M. Origin and Emplacement of Ophiolites. *Rev. Geophys.* **1982**, *20*, 735–760. [CrossRef]
5. Dilek, Y. Ophiolites in Earth history: Introduction. *Geol. Soc. Lond. Spec. Publ.* **2003**, *218*, 9–19. [CrossRef]
6. Sanità, E.; Di Rosa, M.; Marroni, M.; Meneghini, F.; Pandolfi, L. Insights into the Subduction of the Ligure-Piemontese Oceanic Basin: New Constraints from the Metamorphism in the Internal Ligurian Units (Northern Apennines, Italy). *Minerals* **2024**, *14*, 64. [CrossRef]
7. Barbero, E.; Di Rosa, M.; Pandolfi, L.; Delavari, M.; Dolati, A.; Zaccarini, F.; Saccani, E.; Marroni, M. Deformation history and processes during accretion of seamounts in subduction zones: The example of the Durkan Complex (Makran, SE Iran). *Geosci. Front.* **2023**, *14*, 101522. [CrossRef]
8. Hutchison, C.S. *Geological Evolution of Southeast Asia*; Oxford University Press: Londen, UK, 1989.
9. Hall, R. Late Jurassic–Cenozoic reconstructions of the Indonesian region and the Indian Ocean. *Tectonophysics*, 2012; 570–571, 1–41. [CrossRef]
10. Metcalfe, I. Gondwana dispersion and Asian accretion: Tectonic and palaeogeographic evolution of eastern Tethys. *J. Asian Earth Sci.* **2013**, *66*, 1–33. [CrossRef]
11. Zahirovic, S.; Seton, M.; Müller, R.D. The Cretaceous and Cenozoic tectonic evolution of Southeast Asia. *Solid. Earth* **2014**, *5*, 227–273. [CrossRef]
12. Müller, R.D.; Cannon, J.; Qin, X.; Watson, R.J.; Gurnis, M.; Williams, S.; Pfaffelmoser, T.; Seton, M.; Russell, S.H.J.; Zahirovic, S. GPlates: Building a Virtual Earth Through Deep Time. *Geochem. Geophys. Geosyst.* **2018**, *19*, 2243–2261. [CrossRef]
13. Pubellier, M.; Monnier, C.; Maury, R.; Tamayo, R. Plate kinematics, origin and tectonic emplacement of supra-subduction ophiolites in SE Asia. *Tectonophysics* **2004**, *392*, 9–36. [CrossRef]
14. Wang, Y.J.; Qian, X.; Asis, J.B.; Cawood, P.A.; Wu, S.N.; Zhang, Y.Z.; Feng, Q.L.; Lu, X.H. "Where, when and why" for the arc-trench gap from Mesozoic Paleo-Pacific subduction zone: Sabah Triassic-Cretaceous igneous records in East Borneo. *Gondwana Res.* **2023**, *117*, 117–138. [CrossRef]
15. William, P.R.; Johnston, C.R.; Almond, R.A. Late Cretaceous to Early Tertiary structural elements of West Kalimantan. *Tectonophysics* **1988**, *148*, 279–297. [CrossRef]
16. Wang, Y.J.; Qian, X.; Cawood, P.A.; Ghani, A.; Gan, C.S.; Wu, S.N.; Zhang, Y.Z.; Wang, Y.; Zhang, P.Z. Cretaceous Tethyan subduction in SE Borneo: Geochronological and geochemical constraints from the igneous rocks in the Meratus Complex. *J. Asian Earth Sci.* **2022**, *226*, 105084. [CrossRef]
17. Leong, K.M. *The Geology and Mineral Resources of the Upper Segama Valley and Darvel Bay Area, Sabah, Malaysia. Geological Survey Department. British Territories in Borneo (Malaysia)*; US Government Printing Office: Washington, DC, USA, 1974; p. 354.
18. Graves, J.E.; Hutchison, C.S.; Bergman, S.C.; Swauger, D.A. Age and MORB geochemistry of the Sabah ophiolite basement. *Bull. Geol. Soc. Malays.* **2000**, *44*, 151–158. [CrossRef]
19. Wang, Y.J.; Wu, S.N.; Qian, X.; Asis, J.B.; Wang, Y.; Zhang, Y.Z.; Feng, Q.L.; Wang, W.T.; Zhang, P.Z. Early Triassic-Late Cretaceous Paleo-Pacific subduction zone along the East Asia continental margin: Fore-arc igneous records in Sabah of NE Borneo. *Chin. Sci. Bull.* **2023**, *68*, 954–971. [CrossRef]
20. Hutchison, C.S. Stratigraphic-tectonic model for Eastern Borneo. *Bull. Geol. Soc. Malays.* **1988**, *22*, 135–152. [CrossRef]
21. Tjia, H.D. Accretion tectonics in Sabah: Kinabalu suture and East Sabah accreted terrane. *Bull. Geol. Soc. Malays.* **1988**, *22*, 237–251. [CrossRef]
22. Rangin, C.; Bellon, H.; Bernard, F.; Letouzey, J.; Müller, C.; Sanudin, T. Neogene arc-continent collision in Sabah, Northern Borneo (Malaysia). *Tectonophysics* **1990**, *183*, 305–319. [CrossRef]
23. Tongkul, F. Structural styles and tectonics of western and northern Sabah. *Bull. Geol. Soc. Malays.* **1990**, *27*, 227–240. [CrossRef]
24. Schluter, H.U.; Hinz, K.; Block, M. Tectono-stratigraphic terranes and detachment faulting of the South China Sea and Sulu Sea. *Mar. Geol.* **1996**, *130*, 39–78. [CrossRef]
25. Burton-Johnson, A.B.; Macpherson, C.G.; Millar, I.L.; Whitehouse, M.J.; Ottley, C.J.; Nowell, G.M. A Triassic to Jurassic in north Borneo: Geochronology, geochemistry, and genesis of the Segama Valley Felsic Intrusions and the Sabah opiolite. *Gondwana Res.* **2020**, *84*, 229–244. [CrossRef]
26. Swauger, D.A.; Bergman, S.C.; Graves, J.E.; Hutchison, C.S.; Surat, T.; Morillo, A.P.; Benavidez, J.J.; Pagado, E.S. *Tertiary Stratigraphic, Tectonic, and Thermal History of Sabah, Malaysia: Results of a 10 Day Reconnaissance Field Study and Laboratory Analyses*; Unpublished Report TRS TSR; ARCO International Oil and Gas Company: Plano, TX, USA, 1995; pp. 1–61.
27. Hall, R. Cenozoic geological and plate tectonic evolution of SE Asia and the SW Pacific: Computer-based reconstructions, model and animations. *J. Asian Earth Sci.* **2002**, *20*, 353–431. [CrossRef]
28. Hutchison, C.S. Ophiolite metamorphism in Northeast Borneo. *Lithos* **1978**, *11*, 195–208. [CrossRef]
29. Tongkul, F. Tectonic evolution of Sabah, Malaysia. *J. Asian Earth Sci.* **1991**, *6*, 395–405. [CrossRef]
30. Omang, S.A.K.; Barber, A.J. Origin and tectonic significance of the metamorphic rocks associated with the Darvel Bay Ophiolite, Sabah, Malaysia. *Geol. Soc. London Spec. Publ.* **1996**, *106*, 263–279. [CrossRef]

31. Hutchison, C.S. The 'Rajang Accretionary Prism' and 'Lupar Line' problem of Borneo. In *Tectonic Evolution of SE Asia*; Hall, R., Blundell, D.J., Eds.; Geological Society London Special Publication: London, UK, 1996; Volume 106, pp. 247–261.
32. Zheng, H.; Sun, X.M.; Wang, P.J.; Chen, W.; Yue, J.P. Mesozoic tectonic evolution of the Proto-South China Sea: A perspective from radiolarian paleobiogeography. *J. Asian Earth Sci.* **2019**, *179*, 37–55. [CrossRef]
33. Tian, Z.W.; Tang, W.; Wang, P.J.; Zhao, Z.G.; Sun, X.M.; Tang, H.F. Tectonic evolution and key geological issues of the Proto-South China Sea. *Acta Geol. Sin.* **2021**, *95*, 77–90. [CrossRef]
34. Young, A.; Flament, N.; Maloney, K.; Williams, S.; Matthews, K.; Zahirovic, S.; Müller, R.D. Global kinematics of tectonic plates and subduction zones since the late Paleozoic Era. *Geosci. Front.* **2019**, *10*, 989–1013. [CrossRef]
35. Liu, H.; Wang, B.D.; Chen, L.; Li, X.B.; Wang, L.Q. Early Carboniferous subduction of Lungmu Co-Shuanghu Paleo-Tethys Ocean: Evidence from island arc volcanic rocks in Riwanchaka, Central Qiangtang. *Geol. Bull. Chin.* **2015**, *34*, 274–282.
36. Stampfli, G.M.; Hochard, C.; Vérard, C.; Wilhem, C.; Vonraumer, J. The formation of Pangea. *Tectonophysics* **2013**, *593*, 1–19. [CrossRef]
37. Stampfli, G.M.; Borel, G.D. A plate tectonic model for the Paleozoic and Mesozoic constrained by dynamic plate boundaries and restored synthetic oceanic isochrons. *Earth Planet. Sci. Lett.* **2002**, *196*, 17–33. [CrossRef]
38. Wang, D.; Lin, F.C.; Shi, M.F.; Wang, H.; Yang, X.Y. Geological setting, tectonic evolution and spatio-temporal distributions of main mineral resources in South East Asia: A comprehensive review. *Soild Earth Sci.* **2023**, *8*, 34–48. [CrossRef]
39. Hennig, J.; Breitfeld, H.T.; Hall, R.; Nugraha, A.M.S. The Mesozoic tectono-magmatic evolution at the Paleo-Pacific subduction zone in West Borneo. *Gondwana Res.* **2017**, *48*, 292–310. [CrossRef]
40. Morley, C.K. A tectonic model for the Tertiary evolution of strike-slip faults and rift basins in SE Asia. *Tectonophysics* **2002**, *347*, 189–215. [CrossRef]
41. Fuller, M.; Ali, J.R.; Moss, S.T.; Frost, G.M.; Richter, B.; Mahfi, A. Paleomagnetism of Borneo. *J. Asian Earth Sci.* **1999**, *17*, 3–24. [CrossRef]
42. Advokaat, E.L.; Marshall, N.T.; Li, S.; Spakman, W.; Krijgsman, W.; van Hinsbergen, D.J.J. Cenozoic rotation history of Borneo and Sundaland, SE Asia revealed by paleomagnetism, seismic tomography, and kinematic reconstruction. *Tectonics* **2018**, *37*, 2486–2512. [CrossRef]
43. Wang, Y.J.; Liu, Z.; Murtadha, S.; Cawood, P.A.; Qian, X.; Ghani, A.; Gan, C.S.; Zhang, Y.Z.; Wang, Y.; Li, S. Jurassic subduction of the Paleo-Pacific plate in Southeast Asia: New insights from the igneous and sedimentary rocks in West Borneo. *J. Asian Earth Sci.* **2022**, *232*, 105111. [CrossRef]
44. Breitfeld, H.T.; Hall, R.; Galin, T.; Forster, M.A.; BouDagher-Fadel, M.K. A Triassic to Cretaceous Sundaland-Pacific subduction margin in West Sarawak, Borneo. *Tectonophysics* **2017**, *694*, 35–56. [CrossRef]
45. Raschka, H.; Nacario, E.; Rammlmair, D.; Samonte, C.; Steiner, L. Geology of the ophiolite of Central Palawan Island, Philippines. *Ophiolite* **1985**, *10*, 375–390.
46. Gibaga, C.R.L.; Arcilla, C.A.; Hoang, N. Volcanic rocks from the central and southern Palawan Ophiolites, Philippines: Tectonic and mantle heterogeneity constraints. *J. Asian Earth Sci. X* **2020**, *4*, 100038. [CrossRef]
47. Dycoco, J.M.A.; Payot, B.D.; Valera, G.T.V.; Labis, F.A.C.; Pasco, J.A.; Perez, A.D.C.; Tani, K. Juxtaposition of Cenozoic and Mesozoic ophiolites in Palawan island, Philippines: New insights on the evolution of the Proto-South China Sea. *Tectonophysics* **2021**, *819*, 229085. [CrossRef]
48. Labis, F.A.C.; Payot, B.D.; Valera, G.T.V.; Pasco, J.A.; Dycoco, J.M.A.; Tamura, A.; Morishita, T.; Arai, S. Melt-rock interaction in the subarc mantle: Records from the plagioclase peridotites of the southern Palawan Ophiolite, Philippines. *Int. Geol. Rev.* **2021**, *63*, 1067–1089. [CrossRef]
49. Chien, Y.H.; Wang, K.L.; Chung, S.L.; Ghani, A.A.; Iizuka, Y.; Li, X.H.; Lee, H.Y. Age and genesis of Sabah Ophiolite complexes in NE Borneo. *Goldschmidt Abstr.* **2019**, *598*, 18–23.
50. Zhao, Z.G.; Tang, W.; Liu, S.X.; Tang, H.F.; Wang, P.J.; Tian, Z.W. U-Pb zircon ages and petrogeochemistry and tectonic implications of gabbro and granite in southwest Lahad Datu area of Sabah, Malaysia. *Acta Oceanol. Sin.* **2024**, *43*, 94–110. [CrossRef]
51. Wang, Y.J.; Zhang, A.M.; Qian, X.; Asis, J.B.; Feng, Q.L.; Gan, C.S.; Zhang, Y.Z.; Cawood, P.A.; Wang, W.T.; Zhang, P.Z. Cretaceous Kuching accretionary orogenesis in Malaysia Sarawak: Geochronological and geochemical constraints from mafic and sedimentary rocks. *Lithos*, 2021; 400–401, 106425. [CrossRef]
52. Wang, Y.J.; Wu, S.N.; Qian, X.; Cawood, P.A.; Lu, X.H.; Gan, C.S.; Bin Asis, J.; Zhang, P.Z. Early Cretaceous subduction in NW Kalimantan: Geochronological and geochemical constraints from the Raya and Mensibau igneous rocks. *Gondwana Res.* **2022**, *101*, 243–256. [CrossRef]
53. Tongkul, F. The geology of Northern Sabah, Malaysia: Its relationship to the opening of the South China Sea Basin. *Tectonophysics* **1994**, *235*, 131–147. [CrossRef]
54. Jasin, B. Significance of radiolarian cherts from the Chert-Spilite Formation, Telupid, Sabah. *Bull. Geol. Soc. Malays.* **1992**, *31*, 67–83. [CrossRef]
55. Asis, J.; Jasin, B. Aptian to Turonian Radiolaria from the Darvel Bay Ophiolite Complex, Kunak, Sabah. *Bull. Geol. Soc. Malays.* **2012**, *58*, 89–96. [CrossRef]
56. Hall, R. Contraction and extension in northern Borneo driven by subduction rollback. *J. Asian Earth Sci.* **2013**, *76*, 399–411. [CrossRef]
57. Jasin, B. Geological significance of radiolarian cherts in Sabah. *Bull. Geol. Soc. Malays.* **2000**, *44*, 35–43. [CrossRef]

58. Jasin, B.; Tongkul, F. Cretaceous radiolarians from Baliojong ophiolite sequence, Sabah, Malaysia. *J. Asian Earth Sci.* **2013**, *76*, 258–265. [CrossRef]
59. Liu, Y.S.; Gao, S.; Hu, Z.C.; Gao, C.G.; Zong, K.Q.; Wang, D.B. Continental and oceanic crust recycling-induced melt-peridotite interactions in the Trans-North China Orogen: U-Pb dating, Hf isotopes and trace elements in zircons from mantle xenoliths. *J. Petrol.* **2010**, *51*, 537–571. [CrossRef]
60. Andersen, T. Correction of common lead in U-Pb analyses that do not report 204Pb. *Chem. Geol.* **2002**, *192*, 59–79. [CrossRef]
61. Blichert-Toft, J.; Albarède, F. The Lu-Hf isotope geochemistry of chondrites and the evolution of the mantle-crust system. *Earth Planet. Sci. Lett.* **1997**, *148*, 243–258. [CrossRef]
62. Griffin, W.L.; Pearson, N.J.; Belousova, E.; Jackson, S.E.; van Achterbergh, E.; O'Reilly, S.Y.; Shee, S.R. The Hf isotope composition of cratonic mantle: LAM-MC-ICPMS analysis of zircon megacrysts in kimberlites. *Geochim. Cosmochim. Acta* **2000**, *64*, 133–147. [CrossRef]
63. Griffin, W.L.; Wang, X.; Jackson, S.E.; Pearson, N.J.; O'Reilly, S.Y.; Xu, X.; Zhou, X. Zircon chemistry and magma mixing, SE China: In-situ analysis of Hf isotopes, Tonglu and Pingtan igneous complexes. *Lithos* **2002**, *61*, 237–269. [CrossRef]
64. Liu, X.M.; Gao, S.; Yuan, H.L.; Hattendorf, B.; Gunther, D.; Chen, L.; Hu, S.H. Analysis of 42 major and trace elements in glass standard reference materials by 193nm LA-ICPMS. *Acta Petrol. Sin.* **2002**, *18*, 408–418.
65. Yang, Y.H.; Zhang, H.F.; Chu, Z.Y.; Xie, L.W.; Wu, F.Y. Combined chemical separation of Lu, Hf, Rb, Sr, Sm and Nd from a single rock digest and precise and accurate isotope determinations of Lu–Hf, Rb–Sr and Sm–Nd isotope systems using Multi-Collector ICP-MS and TIMS. *Int. J. Mass. Spectrome.* **2010**, *290*, 120–126. [CrossRef]
66. Sun, S.S.; McDonough, W.F. Chemical and isotopic systematics of oceanic basalts: Implications for mantle composition and processes. *Geol. Soc. Lond. Spec. Pub.* **1989**, *42*, 313–345. [CrossRef]
67. Zheng, Y.F. Metamorphic chemical geodynamics in continental subduction zones. *Chem. Geol.* **2012**, *328*, 5–48. [CrossRef]
68. Katayama, I.; Muko, A.; Iizuka, T.; Maruyama, S.; Terada, K.; Tsutsumi, Y.; Sano, Y.; Zhang, R.Y.; Liou, J.G. Dating of zircon from Ti-clinohumite-bearing garnet peridotite: Implication for timing of mantle metasomatism. *Geology* **2003**, *31*, 713–716. [CrossRef]
69. Griffin, W.L.; Graham, S.; O'Reily, S.Y.; Pearson, N.J. Lithosphere evolution beneath the Kaapvaal Craton: Re-Os systematics of sulfides in mantle-derived peridotites. *Chem. Geol.* **2004**, *208*, 89–118. [CrossRef]
70. Smith, D.; Griffin, W.L. Garnetite xenoliths and mantle-water interactions below the Colorado Plateau, Southwestern United States. *J. Petrol.* **2005**, *46*, 1901–1924. [CrossRef]
71. Gao, T.S.; Chen, J.F.; Xie, Z.; Yang, S.H.; Yu, G. Zircon SHRIMP UPb age of garnet olivine pyroxenite at Hujialin in the Sulu terrane and its geological significance. *Chin. Sci. Bull.* **2004**, *49*, 2198–2204. [CrossRef]
72. Yamamoto, S.; Komiya, T.; Yamamoto, H.; Kaneko, Y.; Terabayashi, M.; Katayama, I.; Iizuka, T.; Maruyama, S.; Yang, J.; Kon, Y.; et al. Recycled crustal zircons from podiform chromitites in the Luobusa ophiolite, southern Tibet. *Island Arc* **2013**, *22*, 89–103. [CrossRef]
73. Robinson, P.T.; Trumbull, R.B.; Schmitt, A.; Yang, J.S.; Li, J.W.; Zhou, M.F.; Erzinger, J.; Dare, S.; Xiong, F.H. The origin and significance of crustal minerals in ophiolitic chromitites and peridotites. *Gondwana Res.* **2015**, *27*, 486–506. [CrossRef]
74. Zheng, J.P.; Griffin, W.L.; O'Reilly, S.Y.; Yang, J.S.; Zhang, R.Y. A refractory mantle protolith in younger continental crust, east-central China: Age and composition of zircon in the Sulu ultrahigh-pressure peridotite. *Geology* **2006**, *34*, 705–708. [CrossRef]
75. Hermann, J.; Rubatto, D.; Trommsdorff, V. Sub-Solidus Oligocene Zircon Formation in Garnet Peridotite during Fast Decompression and Fluid Infiltration (Duria, Central Alps). *Mineral. Petrol.* **2006**, *88*, 181–206. [CrossRef]
76. Liati, A.; Gebauer, D. Crustal origin of zircon in a garnet peridotite: A study of U-Pb SHRIMP dating, mineral inclusions and REE geochemistry (Erzgebirge, Bohemian Massif). *Eur. J. Mineral.* **2009**, *21*, 737–750. [CrossRef]
77. Xiong, Q.; Zheng, J.P.; Griffin, W.L.; O'Reilly, S.Y.; Pearson, N.J. Pyroxenite Dykes in Orogenic Peridotite from North Qaidam (NE Tibet, China) Track Metasomatism and Segregation in the Mantle Wedge. *J. Petrol.* **2014**, *55*, 2347–2376. [CrossRef]
78. Shen, T.T.; Zhang, L.F.; Yang, J.S.; Zhang, C.; Qiu, T.; Bader, T. The characteristics and significance of age of zircon from ultramafic rocks: A case study from UHP serpentinites in Chinese southwestern Tianshan. *Acta Petrol. Sin.* **2017**, *33*, 3783–3800.
79. Belousova, E.A.; González Jiménez, J.M.; Graham, I.; Griffin, W.L.; O'Reilly, S.Y.; Pearson, N.; Martin, L.; Craven, S.; Talavera, C. The enigma of crustal zircons in upper-mantle rocks: Clues from the Tumut ophiolite, southeast Australia. *Geology* **2015**, *43*, 119–122. [CrossRef]
80. Liati, A.; Franz, L.; Gebauer, D.; Fanning, C.M. The timing of mantle and crustal events in South Namibia, as defined by SHRIMP dating of zircon domains from a garnet peridotite xenolith of the Gibeon Kimberlite Province. *J. Afr. Earth Sci.* **2004**, *39*, 147–157. [CrossRef]
81. Scambelluri, M.; Cannaò, E.; Guerini, S.; Bebout, G.E.; Epstein, G.S.; Rotondo, F.; Campomenosi, N.; Tartarotti, P. Carbon mobility and exchange in a plate-interface subduction mélange: A case study of meta-ophiolitic rocks in Champorcher Valley, Italian Alps. *Lithos*, 2022; 428–429, 106813. [CrossRef]
82. Song, S.G.; Su, L.; Niu, Y.L.; Zhang, L.F.; Zhang, G.B. Petrological and geochemical constraints on the origin of garnet peridotite in the North Qaidam ultrahigh-pressure metamorphic belt, northwestern China. *Lithos* **2007**, *96*, 243–265. [CrossRef]
83. Zheng, J.P.; Sun, M.; Griffin, W.L.; Zhou, M.F.; Zhao, G.C.; Robinson, P.; Tang, H.Y.; Zhang, Z.H. Age and geochemistry of contrasting peridotite types in the Dabie UHP belt, eastern China: Petrogenetic and geodynamic implications. *Chem. Geol.* **2008**, *247*, 82–304. [CrossRef]

84. Liu, F.L.; Shi, J.R.; Liu, J.H.; Ye, J.G.; Liu, P.H.; Wang, F. Protolith and ultranhigh-pressure (UHP) metamorphic ages of ultramafic rocks in Weihai area, North Sulu UHP terrane. *Acta Petrol. Sin.* **2011**, *27*, 1075–1084.
85. Katayama, I.; Maruyama, S. Inclusion study in zircon from ultrahigh-pressure metamorphic rocks in the Kokchetav massif: An excellent tracer of metamorphic history. *J. Geol. Soc.* **2009**, *166*, 783–796. [CrossRef]
86. Chen, R.X.; Zheng, Y.F. Multiple crust-mantle interaction in continental subduction zones: Insights from orogenic peridoties. *Earth Sci.* **2019**, *44*, 4095–4101. [CrossRef]
87. Yakymchuk, C.; Kirkland, C.L.; Clark, C. Th/U ratios in metamorphic zircon. *J. Metamorph. Geol.* **2018**, *36*, 715–737. [CrossRef]
88. Xiang, W.; Griffin, W.L.; Jie, C.; Pinyun, H.; Xiang, L. U and Th Contents and Th/U Ratios of Zircon in Felsic and Mafic Magmatic Rocks: Improved Zircon-Melt Distribution Coefficients. *Acta Geol. Sin.* **2011**, *85*, 164–174. [CrossRef]
89. El-Bialy, M.Z.; Ali, K.A. Zircon trace element geochemical constraints on the evolution of the Ediacaran (600~614Ma) postcollisional Dokhan volcanics and younger granites of SE Sinai, NE Arabian-Nubian Shield. *Chem. Geol.* 2013; 360–361, 54–73.
90. Pearce, J.A.; Peate, D.W. Tectonic implications of the composition of volcanic arc magmas. *Annu. Rev. Earth Planet. Sci.* **1995**, *23*, 251–285. [CrossRef]
91. Schulz, Z.; Klemd, R.; Brätz, H. Host rock compositional controls on zircon trace element signatures in metabasites from the Austroalpine basement. *Geochim. Cosmochim. Acta* **2006**, *70*, 697–710. [CrossRef]
92. Grimes, C.B.; John, B.E.; Keleman, P.B.; Mazdab, F.Z.; Wooden, J.L.; Cheadle, M.J.; Hanghoj, K.; Schwartz, J.J. Trace element chemistry of zircon from oceanic crust: A method for distinguishing detrital zircon provenance. *Geology* **2015**, *35*, 643–646. [CrossRef]
93. Grimes, C.B.; Wooden, J.L.; Cheadle, M.J.; John, B.E. "Fingerprinting" tectono-magmatic provenance using trace elements in igneous zircon. *Contrib. Mineral. Petrol.* **2015**, *170*, 46. [CrossRef]
94. Tian, Z.W.; Tang, H.F.; Zhao, Z.G.; Tang, W.; He, K.L.; Zhu, C.X.; Wang, P.J. U-Pb dating of detrital zircons from Chert-Spilite Formation in Sabah, Malaysia and its geological significance. *Glob. Geol.* **2021**, *40*, 52–64.
95. Liu, X.J.; Xu, J.F.; Wang, S.Q.; Hou, Q.Y.; Bai, Z.H.; Lei, M. Geochemistry and dating of E-MORB type mafic rocks from Dalabute ophiolite in West Junggar, Xinjiang and geological implications. *Acta Petrol. Sin.* **2009**, *25*, 1373–1389.
96. Wang, J.R.; Chen, W.F.; Zhang, Q.; Jiao, S.T.; Yang, J.; Pan, Z.J.; Wang, S. Preliminary research on data mining of N-MORB and E-MORB: Discussion on method of the basalt discrimination diagrams and the character of MORB's mantle source. *Acta Petrol. Sin.* **2017**, *33*, 993–1005.
97. Schilling, J.G.; Thompson, G.; Kingsley, R.; Humphris, S. Hotspot-migrating ridge interaction in the South Atlantic. *Nature* **1985**, *313*, 187–191. [CrossRef]
98. Zindler, A.; Hart, S. Chemical geodynamics. *Annu. Rev. Earth Planet. Sci.* **1986**, *14*, 493–571. [CrossRef]
99. Niu, Y.L.; Collerson, K.D.; Batiza, R.; Wendt, J.I.; Regelous, M. Origin of enriched-type mid-ocean ridge basalt at ridges far from mantle plumes: The East Pacific Rise at 11° 20′ N. *J. Geophys. Res.* **1999**, *104*, 7067–7087. [CrossRef]
100. Workman, R.K.; Hart, S.R.; Jackson, M.; Regelous, M.; Farley, K.A.; Blusztajn, J.; Kurz, M.; Staudigel, H. Recycled metasomatized lithosphere as the origin of the Enriched Mantle II (EM2) end-member: Evidence from the Samoan Volcanic Chain. *Geochem. Geophys. Geosyst.* 2004; 5, 2003GC000623. [CrossRef]
101. Tang, L.M.; Chen, H.L.; Dong, C.W.; Shen, Z.Y. Triassic neutral and basic rocks in Hainan Island, geochemistry and their geological significance. *Chin. J. Geol.* **2010**, *45*, 1139–1155.
102. Chen, X.Y.; Wang, Y.J.; Han, H.P.; Zhang, Y.Z.; Wen, S.N.; Cao, Y.J. Geochemical and geochronological characteristics of Triassic basic dikes in SW Hainan Island and its tectonic implications. *J. Jilin Univ. Earth Sci. Ed.* **2014**, *44*, 835–847. [CrossRef]
103. Göncüoglu, M.C.; Sayit, K.; Tekin, U.K. Oceanization of the northern Neotethys: Geochemical evidence from ophiolitic melange basalts within the İzmir-Ankara suture belt, NW Turkey. *Lithos* **2010**, *116*, 175–187. [CrossRef]
104. Pearce, J.A. Geochemical fingerprinting of oceanic basalts with applications to ophiolite classification and the search for Archean oceanic crust. *Lithos* **2008**, *100*, 14–48. [CrossRef]
105. Shervais, J.W. Ti-V plots and the petrogenesis of modern and ophiolitic lavas. *Earth Planet. Sci. Lett.* **1982**, *59*, 101–118. [CrossRef]
106. Meschede, M. A method of discriminating between different types of mid-ocean ridge basalts and and continental tholeiites with the Nb–Zr–Y diagram. *Chem. Geol.* **1986**, *56*, 207–218. [CrossRef]
107. Yumul, G.P.; Dimalanta, C.B.; Tamayo, R.; Faustino-Eslava, D.V. Geological features of a collision zone marker: The Antique Ophiolite Complex (Western Panay, Philippines). *J. Asian Earth Sci.* **2013**, *65*, 53–63. [CrossRef]
108. Deng, J.H.; Yang, X.Y.; Zhang, Z.F.; Santosh, M. Early Cretaceous arc volcanic suite in Cebu Island, Central Philippines and its implications on paleo-Pacific plate subduction: Constraints from geochemistry, zircon U–Pb geochronology and Lu–Hf isotopes. *Lithos* **2015**, *230*, 166–179. [CrossRef]
109. Guotana, J.M.R.; Payot, B.D.; Dimalanta, C.B.; Ramos, N.T.; Faustino-Eslava, D.V.; Queaño, K.L.; Yumul, G.P. Arc and backarc geochemical signatures of the proto-Philippine Sea Plate: Insights from the petrography and geochemistry of the Samar Ophiolite volcanic section. *J. Asian Earth Sci.* 2017; 142, 77–92. [CrossRef]
110. Zhou, Y.; Liang, X.Q.; Kröner, A.; Cai, Y.F.; Shao, T.B.; Wen, S.N.; Jiang, Y.; Fu, J.G.; Wang, C.; Dong, C.G. Late Cretaceous lithospheric extension in SE China: Constraints from volcanic rocks in Hainan Island. *Lithos* **2015**, *232*, 100–110. [CrossRef]
111. Shen, L.W.; Yu, J.H.; O'Reilly, S.Y.; Griffin, W.L.; Zhou, X.Y. Subduction-related middle Permian to early Triassic magmatism in central Hainan Island, South China. *Lithos*, 2018; 318–319, 158–175. [CrossRef]

112. Liu, F.; Yang, J.S.; Feng, G.Y.; Niu, X.L.; Li, G.L.; Zhang, C.F. Late Permian to Early Triassic subduction and retreating of the Paleopacific slab: Constraints from continental arc magmatism in Hainan Island. *Acta Petrol. Sin.* **2022**, *38*, 3455–3483. [CrossRef]
113. Zhu, B.Q. Study on chemical heterogeneities of mantle-crustal systems and geochemical boundaries of blocks. *Earth Sci. Front.* **1998**, *5*, 72–80.
114. Yao, J.; Li, S.Q.; He, J.F.; Chen, F.K. Geochemical characteristics of Cenozoic basalts in Tengchong block, the southeastern margin of Qinghai-Tibet Plateau, China: Constraints on the nature of mantle source. *J. Earth Sci. Environ.* **2018**, *40*, 398–413.
115. Hawkesworth, C.; Turner, S.; Peate, D.; McDermott, F.; Calsteren, P. Elemental U and Th variations in island arc rocks: Implications for U-series isotopes. *Chem. Geol.* **1997**, *139*, 207–221. [CrossRef]
116. Wang, Y.J.; Qian, X.; Cawood, P.A.; Liu, H.C.; Feng, Q.L.; Zhao, G.C.; Zhang, Y.H.; He, H.Y.; Zhang, P.Z. Closure of the East Paleotethyan Ocean and amalgamation of the Eastern Cimmerian and Southeast Asia continental fragment. *Earth Sci. Rev.* **2018**, *186*, 195–230. [CrossRef]
117. Wang, Y.J.; Wang, Y.K.; Qian, X.; Zhang, Y.Z.; Gan, C.S.; Senebouttalath, V.; Wang, Y. Early Paleozoic subduction in the Indochina interior: Revealed by Ordo-Silurian mafic-intermediate igneous rocks in South Laos. *Lithos*, 1054. [CrossRef]
118. Wang, Y.J.; Zhang, Y.Z.; Qian, X.; Senebouttalath, V.; Wang, Y.; Wang, Y.K.; Gan, C.S.; Zaw, K. Ordo-Silurian assemblage in the Indochina interior: Geochronological, elemental, and Sr-Nd-Pb-Hf-O isotopic constraints of Early Paleozoic granitoids in South Laos. *Geol. Soc. Am. Bull.* **2020**, *133*, 325–346. [CrossRef]
119. Wang, Y.J.; Qian, X.; Zhang, Y.Z.; Gan, C.S.; Zhang, A.M.; Zhang, F.F.; Feng, Q.L.; Cawood, P.A.; Zhang, P.Z. Southern extension of the Paleotethyan zone in SE Asia: Evidence from the Permo-Triassic granitoids in Malaysia and West Indonesia. *Lithos*, 1063. [CrossRef]
120. Wang, Y.J.; Zhang, Y.Z.; Qian, X.; Wang, Y.; Cawood, P.A.; Gan, C.S.; Senebouttalath, V. Early Paleozoic accretionary orogenesis in the northeastern Indochina and implications for the paleogeography of East Gondwana: Constraints from igneous and sedimentary rocks. *Lithos*, 2021; 382–383, 105921. [CrossRef]
121. Dilek, Y.; Furnes, H. Ophiolite genesis and global tectonic: Geochemical and tectonic fingerprinting of ancient oceanic lithosphere. *Geol. Soc. Am. Bull.* **2011**, *123*, 387–411. [CrossRef]
122. Dilek, Y. Ophiolite concept and its evolution. *Geol. Soc. Am. Spec. Pap.* **2003**, *373*, 1–16.
123. Rampone, E.; Romairone, A.; Abouchami, W.; Piccardo, G.B.; Hofmann, A.W. Chronology, petrology, and isotope geochemistry of the Erro-Tobbio peridotites (Ligurian Alps, Italy): Records of late Palaeozoic lithospheric extension. *J. Petrol.* **2005**, *46*, 799–827. [CrossRef]
124. Reagan, M.K.; Ishizuka, O.; Stern, R.J.; Kelley, K.A.; Ohara, Y.; Blichert-Toft, J.; Bloomer, S.H.; Cash, J.; Fryer, P.; Hanan, B.B.; et al. Fore-arc basalts and subduction initiation in the Izu Bonin-Mariana system. *Geochem. Geophys. Geosyst.* **2010**, *11*, 3. [CrossRef]
125. Yan, Q.S.; Metcalfe, I.; Shi, X.F. U-Pb isotope geochronology and geochemistry of granites from Hainan Island (northern South China Sea margin): Constraints on late Paleozoic-Mesozoic tectonic evolution. *Gondwana Res.* **2017**, *49*, 333–349. [CrossRef]
126. Nguyen, N.T.B.; Satir, M.; Siebel, W.; Vennemann, T.; Long, T.V. Geochemical and isotopic constraints on the petrogenesis of granitoids from the Dalat zone, southern Vietnam. *J. Asian Earth Sci.* **2004**, *23*, 467–482. [CrossRef]
127. Suggate, S.M.; Cottam, M.A.; Hall, R.; Sevastjanova, I.; Forster, M.A.; White, L.T.; Armstrong, R.A.; Carter, A.; Mojares, E. South China continental margin signature for sandstones and granites from Palawan, Philippines. *Gondwana Res.* **2014**, *26*, 699–718. [CrossRef]
128. Shao, L.; Cao, L.; Qiao, P.; Zhang, X.; Li, Q.; van Hinsbergen, D.J.J. Cretaceous–Eocene provenance connections between the Palawan Continental Terrane and the northern South China Sea margin. *Earth Planet. Sci. Lett.* **2017**, *477*, 97–107. [CrossRef]
129. Cui, Y.C.; Shao, L.; Li, Z.X.; Zhu, W.L.; Qiao, P.J.; Zhang, X.T. A Mesozoic Andean-type active continental margin along coastal South China: New geological records from the basement of the northern South China Sea. *Gondwana Res.* **2021**, *99*, 36–52. [CrossRef]
130. Cui, Y.C.; Shao, L.; Yu, M.M.; Huang, C.Y. Formation of Hengchun Accretionary Prism Turbidites and Implications for Deep-water Transport Processes in the Northern South China Sea. *Acta Geol. Sin.* **2021**, *95*, 55–65. [CrossRef]
131. Zhao, Z.G.; Zhang, H.; Cui, Y.C.; Tang, W.; Qiao, P.J. Cenozoic Sea-land Transition and its Petroleum Geological Significance in the Northern South China Sea. *Acta Geol. Sin.* **2021**, *95*, 41–54. [CrossRef]
132. Zhang, G.C.; Feng, C.J.; Yao, X.Z.; Ji, M.; Yang, H.Z.; Qu, H.J.; Zeng, Q.B.; Zhao, Z.; Sun, R. Petroleum Geology in Deepwater Settings in a Passive Continental Margin of a Marginal Sea: A Case Study from the South China Sea. *Acta Geol. Sin.* **2021**, *95*, 1–20. [CrossRef]
133. Cawood, P.A.; Hawkesworth, C.J.; Dhuime, B. Detrital zircon record and tectonic setting. *Geology* **2012**, *40*, 875–878. [CrossRef]